2018

Spurious Grain Formation During Directional Solidification in Microgravity

Supriya Ramashankar Upadhyay
Cleveland State University

SPURIOUS GRAIN FORMATION DURING DIRECTIONAL SOLIDIFICATION IN MICROGRAVITY

SUPRIYA R. UPADHYAY

Bachelor of Engineering in Chemical Engineering

University of Mumbai

MAY 2013

Submitted in partial fulfillment of requirements for the degree

MASTER OF SCIENCE IN CHEMICAL ENGINEERING

at

CLEVELAND STATE UNIVERSITY

MAY 2018

We hereby approve this thesis

For

Supriya R. Upadhyay

Candidate for the Master of Science in Chemical Engineering degree for the

Department of Chemical and Biomedical Engineering

And

CLEVELAND STATE UNIVERSITY'S

College of Graduate Studies by

Thesis Committee Chairperson, Surendra Tewari, Ph.D.

Department of Chemical & Biomedical Engineering

Thesis Committee Member, Orhan Talu, Ph.D.

Department of Chemical & Biomedical Engineering

Thesis Committee Member, Jorge Gatica, Ph.D.

Department of Chemical & Biomedical Engineering

Thesis Committee Member, Christopher Wirth, Ph.D.

Department of Chemical & Biomedical Engineering

Student's Date of Defense: April 30, 2018

DEDICATION

This thesis is dedicated to my parents, Ramashankar and Suman Upadhyay, my family and friends. This would have not been possible without your love, support and encouragement.

ACKNOWLEDGEMENTS

I am immensely grateful to my graduate advisor, Dr. Surendra Nath Tewari for accepting me in his Material Science research team and providing constant guidance and support during my time in Cleveland State University. There is so much to learn from you and you will be forever my inspiration. I indeed feel very blessed to have worked under your supervision and I will definitely cherish this experience all my life.

I would like to thank my committee members: Dr. Orhan Talu, Dr. Jorge Gatica and Dr. Christopher Wirth for taking the time to read my thesis and providing helpful suggestions. I thank Dr. Masoud Ghods for always being supportive and kind to address my questions during my time in the lab. I would also like to convey my sincere thanks to all my colleagues in the lab. I greatly appreciate the support from Ms. Becky Liard, Ms. Darlene Montogomery, and the Chemical and Biomedical engineering staff during my stay in CSU.

I would like to thank my family in India and in the US for their unconditional love and support. I would like to acknowledge all my teachers, friends and colleagues with whom I worked, back in India, for always being encouraging and supporting. I am greatly thankful to all my friends here in the US, who made my stay in Cleveland unforgettable.

Appreciation is expressed to Dr. Richard Grugel of NASA-Marshall Space Flight Center for providing access to raw video image data collected for the PFMI experiments in microgravity. Finally, I would like to thank the Microgravity Materials Research Program at NASA – Marshall Space Flight Center for their continued support of this research.

SPURIOUS GRAIN FORMATION DURING DIRECTIONAL SOLIDIFICATION IN MICROGRAVITY

SUPRIYA R. UPADHYAY

ABSTRACT

This research is aimed at carrying out a systematic investigation of the nucleation, and growth of spurious "misoriented" grains during directional solidification in the low gravity environment of space. Three Al–7 wt. % Si alloy cylindrical samples (MICAST-6, MICAST-7 and MICAST2-12) were directionally solidified on the Space Station at growth speeds varying from 5 to 50 μms^{-1} under thermal gradients varying from 14 to 33 K cm^{-1} in alumina crucibles, under a joint NASA-ESA (European Space Agency) project called, MICAST (Microstructure formation in casting of technical alloys under a diffusive and magnetically controlled convection conditions). The primary purpose of directionally solidifying these three Al-7Si samples in the low gravity environment of space was to eliminate gravity-induced convection in the melt, and grow dendrite array morphology under purely diffusive transport conditions. However, when these directionally solidified samples were extracted from their alumina crucibles, they all showed evidence of surface pores along their length. We believe that these pores formed because in microgravity, there is no imposed force to pull the liquid column down on to the solidifying portion below to continue to feed the volume shrinkage due to liquid to solid phase transformation. There was no additional built-in mechanism, such as a piston and spring, in the MICAST ampoules to keep the melt column pressed onto the solid below. We also believe that even in the absence of gravity, a liquid coulmn which gets detached from the crucible internal waals (forming surface pores), under an imposed positive thermal gradient, would lead to the

liquid-solid surface energy driven Marangoni convection. This convection may fragment fragile secondary or tertiary arms of the primary dendrite trees growing in the mushy zone. These broken dendrite solid fragments may lead to the nucleation and growth of spurious grains in the MICAST samples, where the orientation of primary dendrites would be very different from those in their unmelted seed portions. Our purpose is to examine the longitudinal and transverse microstructures of these MICAST samples to study the formation of spurious grains, and investigate if there is any correlation between the location of the observed surface pores and the formation of spurious grains.

TABLE OF CONTENTS

Page

LIST OF TABLES

Table Page

LIST OF FIGURES

Figure Page

Chapter I

Literature Survey

1.1. Directional Solidification and its Industrial Importance

1.1.1. Directional Solidification

The solidification processing conditions such as thermal gradient, growth speed, and the alloy physical properties such as solute content, phase diagram, etc. determine the microstructure in various solidification processes, such as casting, welding etc. Dendrites are the most common microstructure; they are equiaxed when solidification is carried out in undercooled melt like that during formation of snowflakes or columnar when solidification is carried out under a positive temperature gradient. Some applications require equiaxed grains, such as cast car engines and some require columnar grains, such as gas turbine engine blades[1, 2].

Turbine blades used for high-temperature high-stress applications are fabricated by directional solidification (DS)[3] which requires a constant thermal gradient G [K/cm] and growth speed R [cm/s], to be maintained during DS. These blades are typically multicomponent nickel-based superalloys, comprising a single crystal dendritic structure

with grains oriented parallel to [100] direction along the blade length[2] as shown in Fig. 1(A). During the solidification process, adiabatic conditions are imposed on all sides except the one through which the heat is extracted by moving the alloy containing crucible away from the heat source. A high thermal gradient to growth rate ratio in a binary alloy leads to a planar liquid-solid interface. A low thermal gradient to growth rate ratio causes a two-phase region, mushy zone (mixture of solid and liquid) to be formed between the liquid at the top in the hot end (above the liquidus temperature, and the solid at the bottom in the cold end (below the eutectic temperature) of the mold. The mushy zone in Fig. 1(B) consists of an array of aligned tree-like solid features, called primary dendrites, surrounded by the inter-dendritic liquid. Dendrite morphology[5] and distribution of primary, secondary and tertiary dendrites depend upon the solidification conditions and on the physical properties of the alloy[4].

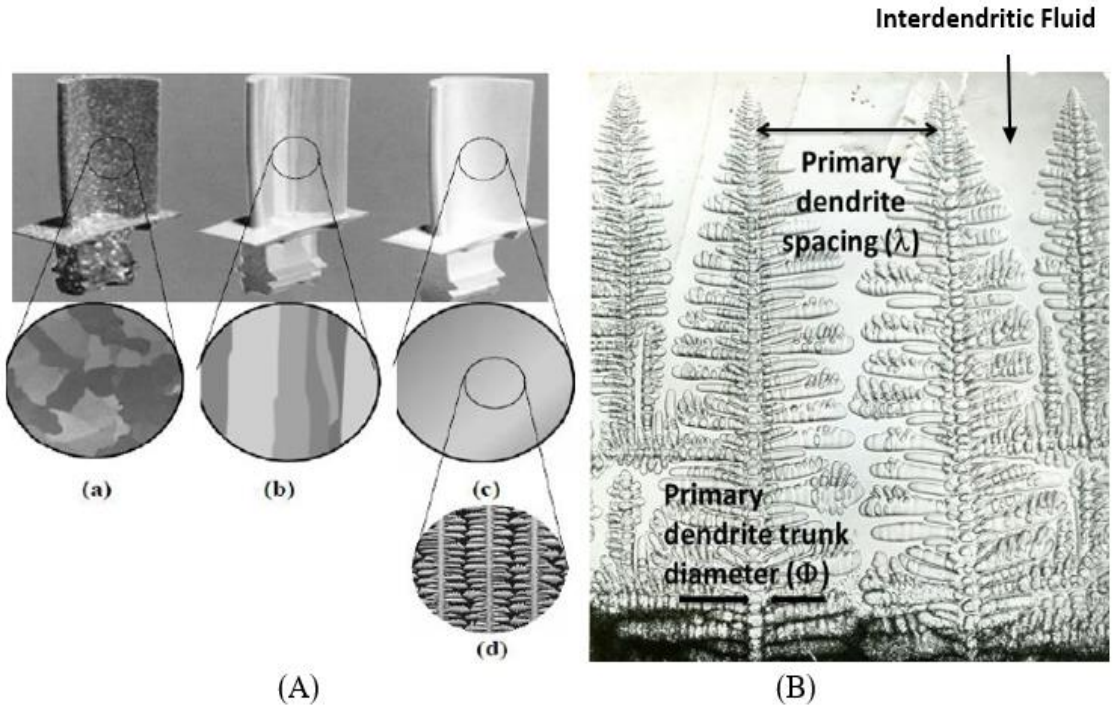

Figure 1 (A) Turbine blade solidified as (a) equiaxed grains (b) columnar grains (c) a single crystal grains (d) Dendritic microstructure of the single crystal turbine blade is represented in the enlarged view[2] (B) SCN -9 wt% H_2O "Transparent alloy" directionally solidified (~ 5μm s^{-1}, ~30Kcm^{-1}) (Dr. Grugel, NASA-MSFC)[6]

1.2. Need for Microgravity

Multiple theories have been proposed[3,7,10-13] and numerous experiments[3,6,8,9] have been conducted to investigate the relationship between primary dendrite arm spacing and the solidification processing parameters like thermal gradient, growth velocity and alloy composition. Since the theoretical models assume diffusive transport environment and the terrestrial experiments are invariably affected by thermosolutal convection, any deviations between the experimental observations and theoretical predictions are simply attributed to the convection[10]. It is now well established that thermosolutal convection during DS of bulk components cannot be eliminated during terrestrial DS irrespective of the alloy compositions selected.

In alloys where solute enrichment increases melt density, such as, Al-19% Cu, a "steepling" type convection[6] is seen, as shown in Fig. 2(a). Notice the non-uniformity of dendrites across the sample cross-section. In alloys where solute enrichment decreases melt density, "plume" type of thermosolutal convection[6] occurs, as typically shown in Fig. 2(b). Please note the dark looking "freckle" defect at about 12:05 PM location in the microstructure. Hence, several low gravity experiments have been conducted in space for the sole purpose of obtaining dendrite array morphology growing under diffusive transport condition having undergone solidification in the absence of convection[8] so that the observed microstructural details can be compared with predictions from available theoretical models.

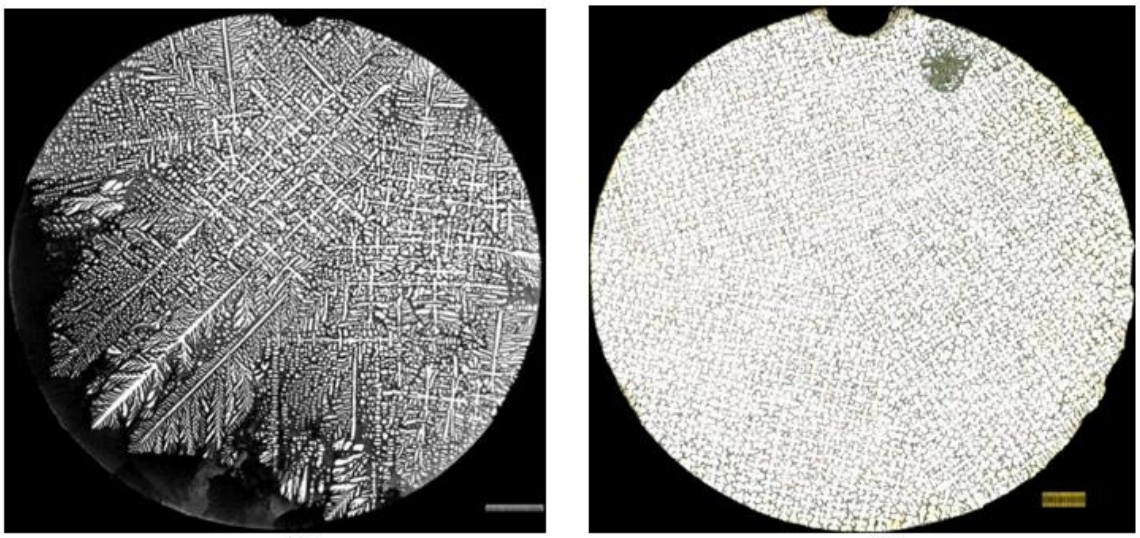

Figure 2 (a) Image of transverse slice of an Al-19 % Cu alloy, grown at 10 μm s^{-1} [3]. This depicts an example of transverse phase macrosegregation. (b) Image of transverse slice of a Pb-6 % Sb alloy, grown at 10 μm s^{-1}. This depicts an example of channel formation as because of plume type thermos-solutal convection[14].

1.3. Why MICAST?

The purpose of MICAST series of experiments was to directionally solidify Al-7Si alloy along [100] direction in the absence of natural convection and compare the primary dendrite spacing to those of the terrestrially grown samples having initial aligned dendritic array, solidified in the presence of convection. Other aim was to compare these spacings with the predictions from theoretical models which assume diffusive transport. As shown schematically in Fig. 3, remelting of a single crystal seed having [100] dendritic alighment and its subsequent DS in the absence of convection would result in maintaining the same dendrite alignment along the entire sample length. It should also not produce any radial or longitudinal macrosegregation because of lack of thermosolutal convection caused by gravity.

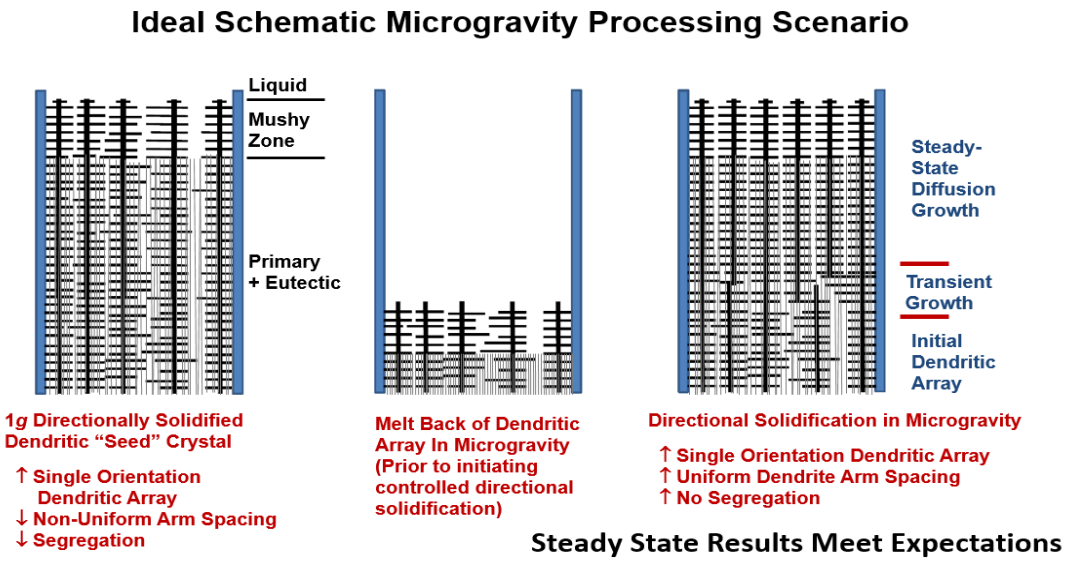

Figure 3 Expected Results of the Directional Solidification conducted in Microgravity[15]

These experiments were designed to help us investigate the role of gravity induced convection on the dendritic network and spacing and on the macrosegregation by comparing the samples solidified on the space station in the absence of convection with those grown terrestrially in the lab in the presence of natural convection. The observed primary dendrite spacings in the three samples (MICAST-6, MICAST-7 and MICAST2-12) appear to agree with predictions from the theoretical models which consider only diffusive transport. However, a careful examination of microstructures shows grains having dendrites which deviate from the [100] orientation of the seed. Such grains are called "spurious grains".

1.4. Spurious (Misoriented) Grains

Ideally the primary dendrite arrays should be perfectly aligned along [100] direction along the entire length of the directionally solidified blades to achieve the highest high temperature rupture strength and therefore the engine operating life. Presence of any misoriented "spurious grain" seriously degrades the elevated temperature creep life and

leads to early blade failure. The presence of spurious grains is the major cause of rejection of the single crystal blades manufactured by industry.

1.4.1. Mechanisms of Spurious Grain Formation

(1) Undercooling in melt

(2) Fragmentation of side arms due to convection

  (a) Mechanical fracture and transport

  (b) Solutal-remelting and transport

  (c) Section change induced flows

  (d) Void induced convection

Extensive studies have been conducted on understanding the mechanism of formation of the misoriented grains in directionally solidified samples. Sometimes, the melt in the solidifying alloy sample gets locally undercooled due to various reasons. This leads to independent nucleation of solid grains which have orientations very different than the primary dendritic network. The final solidified crystal therefore shows the presence of such misoriented grains.

Spurious grains are also generated through forced convection during directional solidification[16]. Constant Stirring during solidification can cause mechanical breaking of the secondary arms or even tertiary at times. These broken fragments may rise, or sink depending on the density difference between the solid formed and the surrounding melt and thus develop into spurious grains if they are not entrapped within the primary dendrites growing around them. Such broken fragments align themselves in different direction and hence the new stray grains do not possess the original orientation of the solidified portion.

Another method of spurious grain formation can be via gravity induced natural thermosolutal convection assisted re-melting and fragmentation at the roots of side branches due to the local solutal enrichment. Such fragmented dendrites are extensively observed inside the "freckle-regions"[6] formed due to rising plumes during processing conditions which favor density inversion in the mushy zone. The convection causes the solute-rich, lower-melting point, liquid in the mushy-zone to flow upwards where it encounters the side-branches that had already formed at higher equilibrium temperatures. The incoming solute rich melt remelts and thus fragments some of these branches[9, 10,17]. Such side-branch fragmentation has been seen during melt back of bulk samples[8], and also as a consequence of decelerating growth speed[18-20].

Spurious grain formation at the cross-section expansion has also been observed in directionally solidified alloys[1]. As the mushy zone grows from smaller portion of the mold into the increased cross-section portion of the mold above, it expands to fill the space by side-ways growth of the secondary arms of the peripheral primary dendrites. The tertiary arms coming off these side-branches grow along the same direction as the primary dendrites in the narrow cross-section below. However, since the platform corners are more prone to efficient heat extraction, melt in this region gets undercooled which leads to the nucleation of solid phase. Spurious grains form from these independently nucleated solid particles. Spurious grains are observed to form preferably on the edges of the thin platform sections of the gas turbine blades directionally solidified in ceramic shell molds[11-13, 21, 22]. Three dimensional numerical simulations demonstrating this mechanism have been attempted using Cellular Automaton[11-13, 22] and the results obtained are in agreement with the experimental results.

The above explained mechanisms are based on experiments conducted on earth, in presence of gravity which enable the convection and buoyancy effects, causing floating or settling of dendritic arms. The phenomenon of melt undercooling has been modelled earlier, however, three-dimensional modeling of thermosolutal-convection-assisted fragmentation and rotation of these dendrite fragments leading to the formation of spurious grains has not been studied. Studies relevant to this area have simplified the case through analytical/ heuristic assumptions and correlations[23]. During directional solidification in the microgravity environment of space in constant diameter ampoules melt undercooling cannot occur. In addition side-arm fragmentation is not expected to occur because there is no convection present in the absence of gravity. Therefore, alloy samples directionally solidified on the Space Station are not expected to contain any spurious grains.

However, if there are pores or bubbles present during directional solidification, then another potential mechanism for fluid flow leading to the side-arm fragmentation becomes possible, the Marangoni convection caused by the gradient in the liquid-vapor surface energy associated with the thermal gradient on the free surface.

1.5. Marangoni Convection

Marangoni convection is the tendency for heat and mass to travel to a gradient of surface tension (σ) at the interfaces between two phases, especially at a liquid-gas interface, causing a flow to occur. Liquid-vapor surface tension changes associated with solute concentration gradient cause solutocapillary Marangoni convection, and those associated with thermal gradient are called thermocapillary Marangoni convection[24]. Marangoni convection has been extensively studied during directional solidification of semiconducting materials by a process called Czochralski crystal growth.

The magnitude of the Marangoni convection is directly related to the temperature gradient in the direction tangential to the interface[25]. The variation of surface tension, σ with temperature (T) and composition (c) can be denoted as below:

$$d\sigma = \frac{\partial \sigma}{\partial T} dT + \frac{\partial \sigma}{\partial c} dc \qquad [1]$$

$\Upsilon = \left| \frac{d\sigma}{dT} \right|$ is the thermal dependence of the surface tension in N/m/K. Similarly, concentration dependence of surface tension can be defined. Thermocapillary convection or thermally induced Marangoni convection expresses the normal component of the shear stress in terms of the tangential derivative of the temperature. For an incompressible fluid with no pressure contribution in a laminar flow, it is written as:

$$[\mu(\nabla \vec{u} + (\nabla \vec{u})^T)].\vec{n} = \Upsilon \nabla_t T \qquad [2]$$

This is a boundary condition that acts at the free surface of the fluid (typically a gas-liquid interface) modeled with the Navier-Stokes equations[26].

The *Marangoni number, Ma* can be expressed as the ratio between the thermocapillary effect and the viscous forces.

$$\mathrm{Ma} = \frac{|\Upsilon| \mathrm{L} \Delta \mathrm{T}}{\mu \kappa} \qquad [3]$$

where L is the length scale of the system in m, ΔT is the maximum temperature difference across the system in K, μ is the dynamic viscosity in kg/s/m, and κ is the thermal diffusivity in m^2/s.

Equation [3] can be rearranged to obtain the following.

$$\mathrm{Ma} = \frac{\sqrt{\frac{\gamma \Delta T}{\rho L}}\sqrt{\frac{\gamma \Delta T}{\rho L}}}{(\nu/L)(\kappa/L)} \quad [4]$$

Here ν is the kinematic viscosity in m^2/s.

The typical velocities involved are the thermocapillary velocity $\sqrt{\frac{\gamma \Delta T}{\rho L}}$, the thermal diffusion velocity(κ/L), and the molecular diffusion velocity(ν/L). An equivalent Reynolds number can also be derived as: $Re = \sqrt{Ma/Pr}$ where $Pr = \nu/\kappa$ is the Prandtl number, which is characteristic of the fluid of interest. Geometry plays an important role in characterizing the flow as it directly influences the Reynold's number and also the Marangoni number. A Marangoni number above $1 \cdot 10^5$ [24] will typically develop unsteady flows, if not turbulent. The Marangoni effect has been observed and accounted for in various surface chemistry applications and fluid flow processes.

Spurious grain due to Marangoni Convection caused by the surface tension gradient in the presence of void on the surface can be better understood with the help of schematic representation shown in Fig. 4. Because of a bubble adhered to the wall (Fig. 4(a)) and the existing thermal gradient, the flow due to Marangoni convection (indicated by arrows in Fig. 4(a)) would bring hot liquid towards the branches of growing primary dendrites. During sample melt back prior to starting the DS, as the primary dendrites melt back (Fig. 4 (b)) their side-arms can get detached from there root (marked as "A") because of the sharp local curvature existing there.

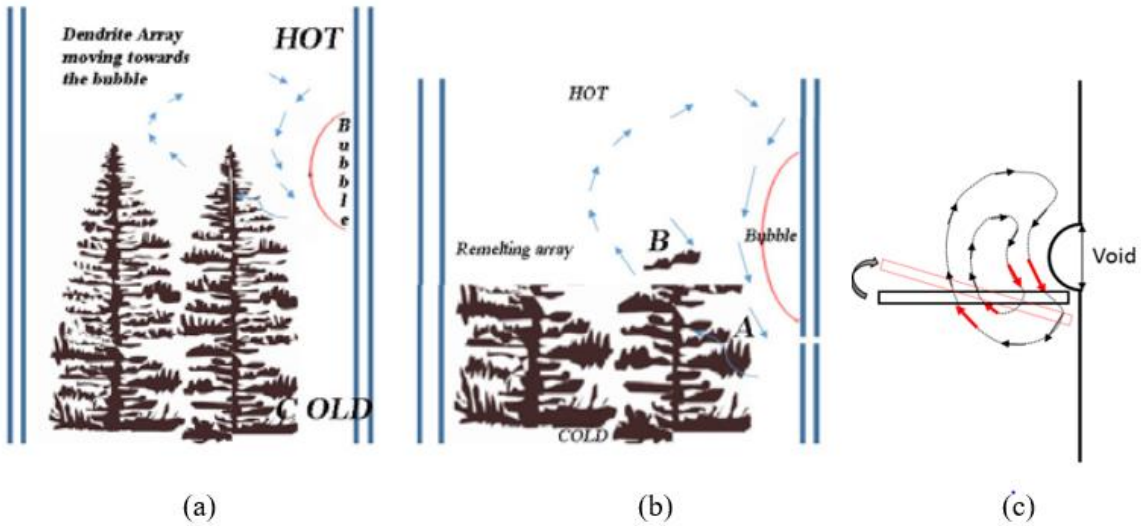

Figure 4 (a) Dendritic array moving towards the bubble (b) Melt back of primary dendrites (c) Rotation of side arm

When the flow moves back upward, it would carry solute-rich lower-melting-point liquid towards the already solidified side-branches. This can also initiate re-melting and fragmentation of the side-branches. The fragmented piece (for example marked as “B”) can get rotated under the repeated impacts of the Marangoni flow stream lines, as represented by the black fragmented feature getting rotated into a very different orientation indicated by the red feature. These misoriented fragments can grow and develop into spurious grains during subsequent directional solidification.

Chapter II

Purpose of Research

Understanding spurious grain formation by Marangoni convection it-self has gained considerable attention recently, because of its adverse effect on microstructure during laser assisted direct metal deposition to repair and salvage the high value nickel and titanium alloy engine components [27-30.]

Primary observation of these MICAST samples showed voids on the surface while image analysis confirmed the presence of spurious grains. We believe that these spurious grains in the MICAST samples must have formed by the dendrite fragmentation phenomenon, except that it was the Marangoni convection arising from the voids present on the surface of the liquid column in regions where the melt got detached from the ampoule wall, which was responsible for the remelting of the dendrite side arms and their rotation.

The purpose of this research is to investigate the influence of Marangoni Convection in the formation of spurious grains in directionally solidified Al-7Si alloy (MICAST Experiment) on the space station in the absence of gravity.

This involved studying one of the earlier low gravity experiments conducted by NASA[31], on the Space Shuttle. Series of these experiments called Pore formation and Mobility Investigation (PFMI) used SCN-0.24 wt. pct. H_2O, an organic transparent alloy of which solidifies in the same manner as Face Centered Cubic metals. Their solidification behavior was recorded in the form of video during many cycles of remelting and directional solidification in micro-gravity. These samples also contained nitrogen. In my research, a review of several of these PFMI experiments was carried out in order to locate the specific portions of PFMI videos which were of our interest, for example where the dendrite array was growing or remelting in the presence of a surface-adhered bubble. As presented below, these experiments clearly showed presence of side-arm remelting and their rotation via the mechanism hypothesized in Fig.4.

The proposed research included

(i) Serial transverse sectioning of MICAST samples and use of video images from PFMI experiments,

(ii) Simulation (COMSOL) of SCN-0.24H_2O and Al-7Si dendrite array while it is growing in the presence of surface voids/pores, and

(iii) Quantitative comparison between the experimental observations and simulation results.

2.1. Methodology

2.1.1. MICAST (Al-7Si Alloy)

Transverse and longitudinal sections from the Al-7Si alloy samples directionally solidified in the space under the MICAST-program (MICAST-6, 7 and 2-12) were metallographically examined. The precise locations where the spurious grains formed were

determined by serial sectioning and metallography at appropriate locations along the sample length. The geometry and location of surface pore with respect to the location of spurious grains was also determined. The angles between primary dendrite array in the seed portion and those within the misaligned grains were measured by EBSD analysis (where appropriate) and also using Image analysis software, ImageJ. Such data were generated in locations, (i) where mushy-zone existed during initial sample remelting stage, (ii) where the array was during growth at a constant speed, and (iii) also where there was an abrupt decrease in the growth speed.

2.1.2. Succinonitrile-0.24% H_2O alloy

PFMI videos[32] were used to extract data regarding solidification conditions (re-melting speed, thermal gradient, location of the dendrite array with respect to the adhered bubble, etc.) and array characteristics (primary spacing, side-branch dimension, dendrite tip radius, etc.) at locations where fragmentation of dendrite side-arms was observed during sample re-melting stage. This was done using ImageJ. Fluid velocity and its variation along several stream contours associated with the Marangoni convection was also measured from such video-data. Dimensions and locations of the fragments rotating under the influence of convection was measured and compared with simulation results.

Chapter III

Experimental Procedure

3.1. MICAST Al-7Si Directionally solidified on space station

3.1.1. Microgravity Processing

Rods of Al-7Si alloy were casted using copper mold after the alloy was prepared by induction melting under argon. Remelting and subsequent directional solidification was carried out on earth in graphite crucible mold having outer and inner diameters as ~ 19 mm and ~ 9 mm, respectively. The graphite mold was inside a quartz tube connected to a vacuum system that achieved a pressure of ~ 10^{-4} torr. These rods were then withdrawn at 20 μm s^{-1} under a thermal gradient of 40 K cm^{-1} to obtain 30 cm long, 9.5 mm diameter dendritic feed-rods. On conducting metallographic examination of the cross-sections, an uniform single-crystal dendritic array having a <100> orientation was revealed. The fraction eutectic measurements carried out on transverse sections along the length of one of the samples showed that there was no macrosegregation along their length. The rods were then machined to obtain 24.5 cm long and 7.8 mm diameter cylinders so that they can be inserted into the ESA supplied alumina flight-crucibles. 12 thermocouples were placed along the groove machined on the external surface of these alumina crucibles. The alumina

crucible with the attached thermocouple was then inserted into a Sample Cartridge Assembly (SCA) which was used by astronauts on the Space Station. A typical SCA is shown in Fig. 5(a). Each sample had its own SCA. ESA's Low Gradient Furnace (LGF)[33] shown in Fig. 5(b) was used to conduct directional solidification. This Bridgman-type furnace (LGF) is contained in a vacuum chamber (the shiny circular door-like feature in the middle right view of the NASA's Materials Science Research Rack (MSRR)). All the three Al-7Si samples, MICAST-6, MICAST-7, and MICAST2-12, were processed at gravity levels below 10^{-4} g in space.

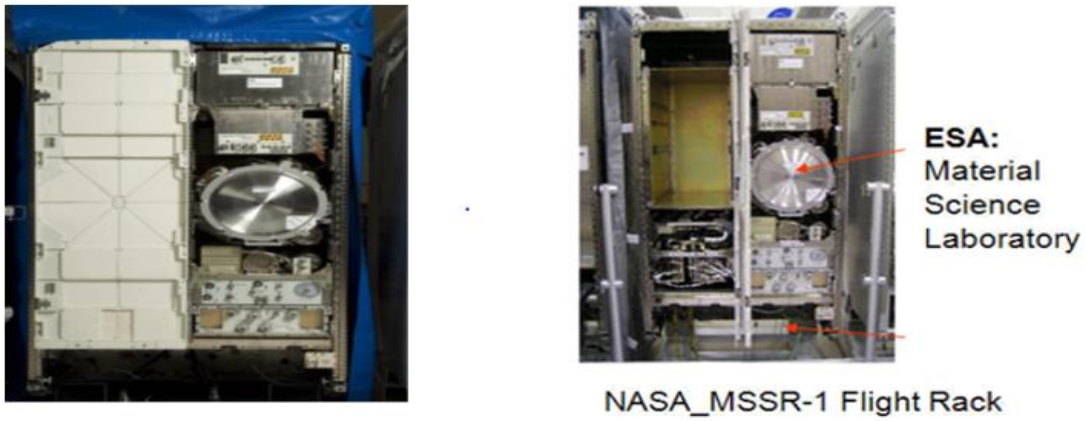

Figure 5 Microgravity Science Research Facility on the International Space Station[33]

Figure 6 (a) ESA_MSL Low Gradient Furnace (LGF) used for the directional solidification and (b) Sample Cartridge Assembly (SCA), in which a sample for a directional solidification experiment on the ISS is contained[33]

During these experiments, initially, the sample was held stationary while the furnace was kept away from the SCA. The furnace was then brought to an initial temperature during processing and translated to remelt ~11 cm of the sample such that the original <100> orientation of the seed crystal does not get disrupted. The temperature in the hot zone was slowly increased to the desired set-point and thermal equilibrium was established by holding the furnace stationary for 2 hours for MICAST-6, and less than 1 hour for MICAST-7 and MICAST2-12 samples. The thermal gradients achieved in the mushy zone were approximately 18.5 K cm^{-1}, 24 K cm^{-1} and 26 K cm^{-1} for MICAST-6, MICAST-7 and MICAST2-12, samples respectively. Finally, the three samples were then directionally solidified by withdrawing the furnace at constant speeds, which ranged from 5 µm s^{-1} to 50 µm s^{-1} depending on the experiment[34].

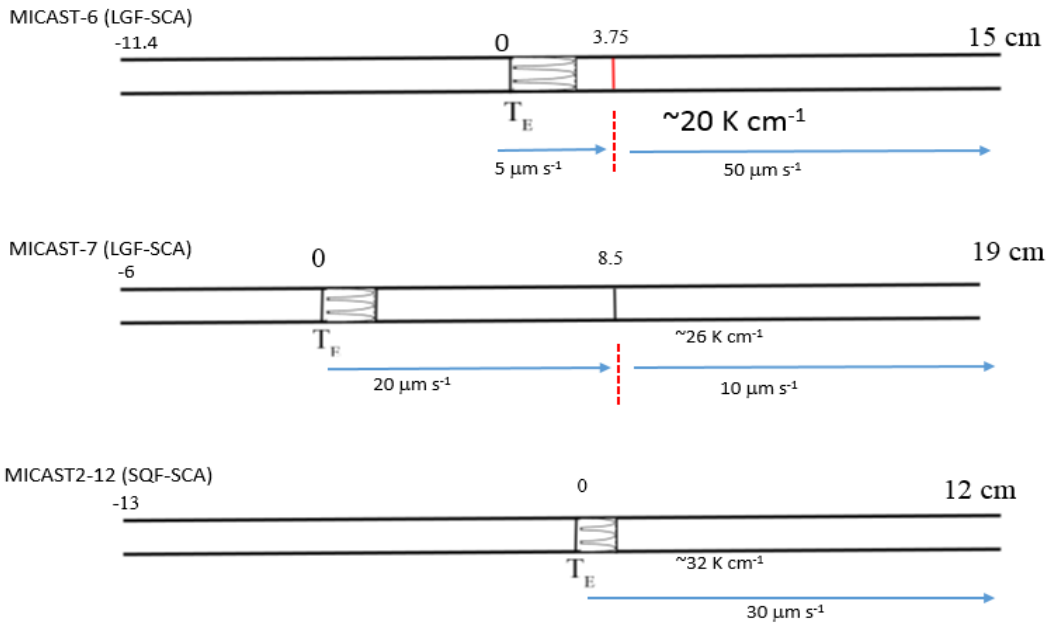

Figure 7 Processing conditions during DS for MICAST-6, MICAST-7 and MICAST-2-12 samples

3.1.2. Microstructural Characterization

After their return to NASA, the directionally solidified MICAST samples were extracted from the alumina crucible. X-ray radiography was carried out while the samples were within the alumina crucible at several rotations. The samples were then extracted and examined. Longitudinal and transverse optical metallography was carried out to examine the microstructures. After a thorough examination of the longitudinal microstructure, several transverse sections were cut along the sample length for examination of the dendrite array morphology and to carry out fraction-eutectic (f_E) measurements.

3.1.2.1. Cutting, mounting, polishing and imaging. The specimens were mounted in a thermosetting epoxy with the help of mounting press at 21 MPa and 120 degrees after curing for 5 minutes. The mounting cylinder and cap were greased with silicone oil prior to sample mounting. After hardening, the samples were engraved with their IDs. These were then ground and polished in a Buehler automatic grinder and polisher, by using abrasive grits of various grades, culminating into a 0.05 micron colloidal silica polish. Typical grinding and polishing steps are shown in Table.1.

Table 1 Grinding and Polishing Steps

Grade	Force/ Sample	Time (min)	RPM
400 (Grinding)	3 lbs	1	120
600 (Grinding)	3 lbs	1	120
800 (Polishing)	3 lbs	2	120
1200 (Polishing)	3 lbs	2	120
0.05μm (Fine polish)	4 lbs	8	120

The polished samples were some-times etched to create better contrast than the polished surface. The etchant was made up of 190 ml of distilled water, 2ml of Hydrochloric acid, and 5 ml of Nitric acid and 2 ml of Hydro fluoric acid. The cotton swab was placed in the etchant solution for soaking. The polished surface was then rubbed gently with the cotton swab for about 5 to 10 seconds and the sample was placed under the cold water stream[35].

With the help of HL Image++ 98 software the optical images were taken at 50-X magnification. Usually 60 to 70 individual pictures were required to cover the entire cross-section of the 9-mm diameter samples and create a montage for subsequent image analysis.

3.1.2.2. Image analysis. The montages were analyzed using an open source image analysis software 'ImageJ' which can be used for measuring primary dendrite trunk diameter, nearest neighbor spacing, fraction eutectic, dendritic orientation etc.

3.1.2.3. Grain orientation & grain boundary analysis. Based on the orientation of the primary dendrites in the given sample, grain boundaries are marked in such a way that dendrites with similar orientation are included in one particular grain. Thus, the basic deciding factor for any grain boundary is the orientation of all dendrites within that grain. A longitudinal groove was machined along the sample length to help align transverse views along the DS direction. The procedure for marking the grain boundaries is as follows:

1. Cross-section images were always aligned such that the sharp-crack was at the 90^{o} location in the montage.

2. Through visual observation, grain boundaries are marked following a color code. For example, Grain 1 Boundary: Yellow, Grain 2 Boundary: Red, Grain 3 Boundary: Green etc. This is then saved as a ROIset (ROI: Region of Interest)
3. Marking the crosses (primary as well as secondary side arms for single dendrite) and saving them as another ROI.
4. Using the ROI of the crosses, the center of each dendrite is found through a macro code (Appendix A) followed by measurement of orientation of the dendrites. It is assumed that at least one arm of either of the primary or secondary dendrites lie in the first quadrant.
5. If the center of the dendrites lies in a particular ROI, it is placed under the corresponding grain category and color scheme is followed again.
6. As a result, images with distinguished grain boundaries and colored dendrites are obtained.

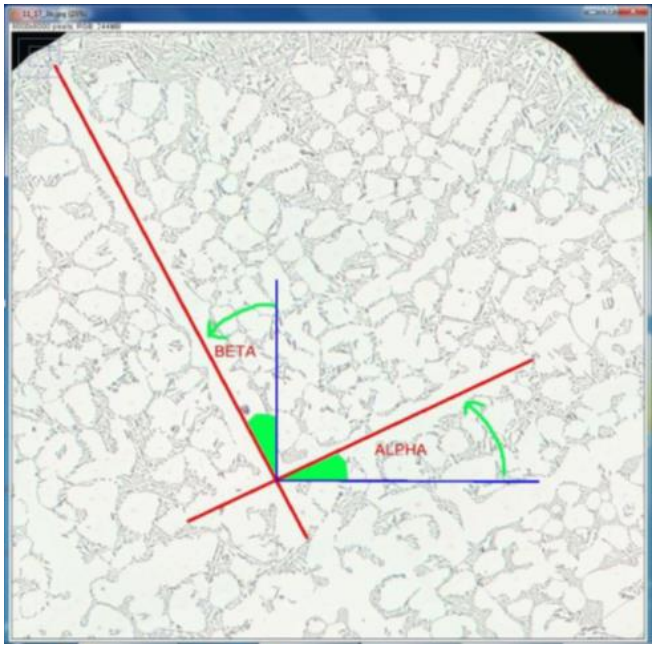

Figure 8 Screen capture of bounding rectangle measurement for arm length and orientation[6]

The above procedure helps in thorough examination of the directionally solidifying grains by observing the trend in grain boundary displacement along the sample DS length on successive serial cross-sections using ImageJ. Other results that were obtained include the ratio of the lengths of both sides of the primary as well secondary arms of the dendrite, difference in the orientation of primary and secondary arms (α and β).

3.1.2.4. Measurement of trunk diameter. Two lines crossing the trunk are drawn and the center of the dendrite is marked using a code which also yields Trunk diameter measurements along with the nearest neighbor spacing etc. Primary trunk diameters were measured and compared with the corresponding theoretically predicted values (model developed by Tewari et al) [36] for all MICAST samples. These results are presented in Appendix B.

3.2. Pore Formation And Mobility Investigation (PFMI)

In 2002, NASA carried out a series of PFMI experiments[31] using a transparent organic alloy, SCN-0.24 H_2O which solidifies with dendritic arrays similar to that of the FCC metals. Purpose of these experiments was to examine pore formation and migration through the mushy-zone.

3.2.1. Experimental Procedure

SCN-0.24 H_2O was filled in a 30 cm long, 10 mm diameter quartz ampoules as shown in Fig. 9. Nitrogen bubbles were injected into the sample tube while filling the sample as a source of porosity in this microgravity experiment. The alloy physical properties[37] are reported in previous microgravity experiments [38, 39]. These ampoules were inserted into the directional solidification furnace shown in Fig. 9.

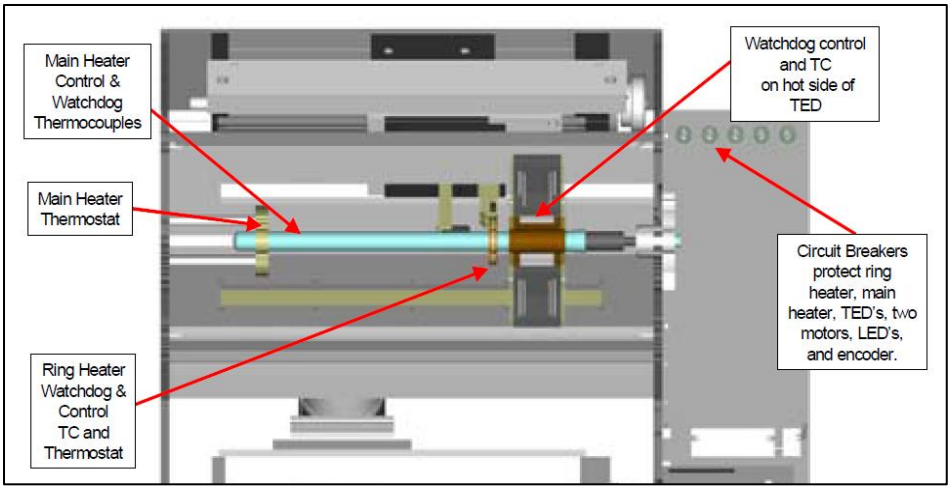

Figure 9 Experimental set up for PFMI[40] (Grugel et al 2001, 2004; Spivey et al 2003)

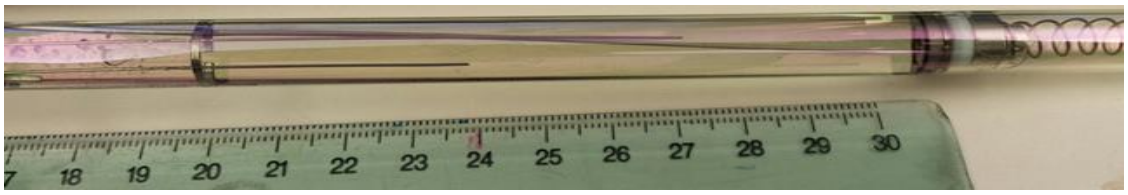

Figure 10 SCN filled quartz tube, thermocouple arrangement[40]

The crucible containing several thermocouples is inserted into the processing unit which houses the translation device and recording cameras (Fig. 9). The indium-tin coated ampoule (color-coded light blue in Fig. 9) consisted of an effective "spring and piston" to account for the thermal expansion and contraction of the sample. The coating helped in heating the ampoule to create thermal gradients. Two video cameras set orthogonal to each other and also to the sample tube help in tracking and recording the bubble movement. Information regarding time, stage position, and temperatures are imprinted on the video. The experiments were entirely monitored from the ground and parameters were set and watched through telescience commanding.

As per Dr. Grugel (private communication), both TC 5 and TC 6 are at the same position in the hot end and would record the same temperature. Hot zone is considerably isothermal over a reasonable distance. TC 1 would be in the cold zone apparently and

would not change temperature. Distance between TC tips: 3 cm, except for TC 5 and 6, which is zero. In the picture of PFMI-15, videos, which we utilized extensively, one can see TC's 6, 5, 4, 3, and the very tip of 1.

Bubble Migration

Bubbles present in a fluid migrate in response to the temperature gradient induced thermocapillary effect as described below[41]:

$$V = \frac{\Delta T . r . \frac{d\gamma}{dT}}{\eta} \quad [5]$$

Here, V is the growth velocity, ΔT is the temperature gradient, r is the bubble radius, dγ/dT is the variation in surface tension with temperature, and η is the dynamic viscosity of the liquid.

Chapter IV

Results and Discussion

4.1. MICAST Experiments (Al-7Si Alloy)

Fig. 11 shows the surface appearance of MICAST 6, 7 and 12 samples after they were extracted from the alumina crucible. The left most arrows indicate the location of the eutectic isotherm after the remelting and at the onset of directional solidification. The reaction between the alloy melt and the alumina crucible are visible as white looking features in the figures. There are portions of the sample where the liquid column seems to have detached from the crucible resulting in depressions (or pits) on the sample surface. Table-2 identifies the locations of the transverse sections made with respect to the Eutectic isotherms in the MICAST-6 sample, and the corresponding growth speed and the thermal gradients in liquid (G_l) and in mushy zone (G_m) at those locations during directional solidification.

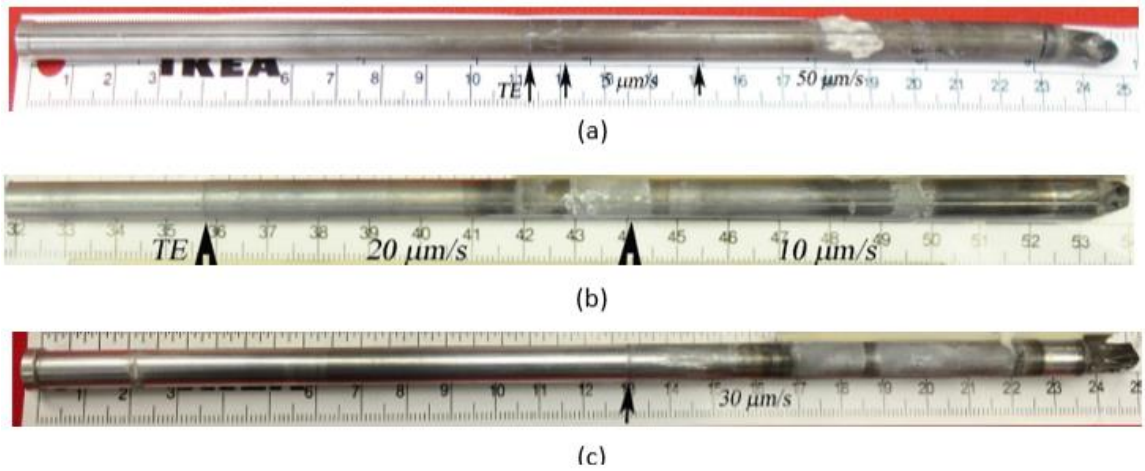

Figure 11 DSed samples obtained from space station (a) MICAST 6 (b) MICAST 7 (c) MICAST 12

4.1.1. MICAST-6

Table 2 Growth Conditions and Sample Location for MICAST-6

Sample ID	Distance from the Eutectic Isotherm (mm)	Velocity (um/s)	G_l (K/cm)	G_m (K/cm)
M6-3	-6.7			
M6-7	34.5	5.4908	22.183	19.9415
M6-8L-4	41.147	5.5562	22.18	20
M6-8L-3	44.818	5.5943	22.156	20.078
M6-8L-2	50.42	5.5029	22.069	20.1345
M6-8L-1	54.4	5.4139	22.018	20
M6-9T	60	12.27	21.725	19.6125
M6-10L-1	65.828	28.172	20.622	19
M6-10L-2	70.109	34.289	20.161	18.7805
M6-10L-3	73.8	38.191	19.82	18.19
M6-11T	82.36	44.748	18.969	18.1345
M6-12L-10	93.04	51.868	17.67	17.235
M6-12L-1	93.325	52.035	17.631	17.2155
M6-12L-2	98.026	55.377	16.886	
M6-12L-3	102.037	58.641	16.078	16.489
M6-12L-4	106.438	62.734	15.022	
M6-12L-5	110.199	67.87	13.925	18.15

Fig.12 shows dendrite orientations in various grains on several transverse locations along the DS length of MICAST-6 sample.

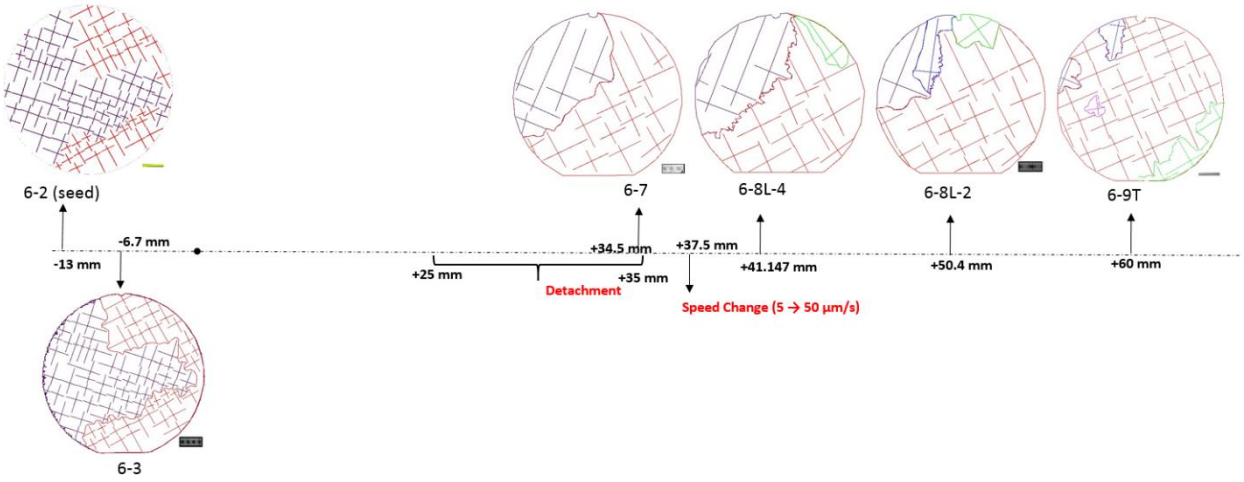

Figure 12 Results of image analysis on microstructures of MICAST-6

There are 2 grains in the unmelted seed portion of the sample (6.7 mm below the eutectic isotherm). The same two grains are present at 34.5 mm. During directional solidification of this sample, there was a speed change from 5 to 50 μms^{-1}at 37.5 mm location. New misoriented grain (dendrite colored- green), however has appeared at 41 mm. Spurious grains are seen in sections at 50.4 and 60 mm. Since the sample was directionally solidified under microgravity, there would be no convection present. Hence the dendrites in the seed portion should have continued to grow with their original orientation along the entire sample length. What is causing the formation of these spurious grains?

4.1.2. MICAST-7

Table-3 lists locations of the transverse sections in the MICAST-7 sample, and the corresponding growth speed and the thermal gradients at these locations.

Table 3 Growth Conditions and Sample Location for MICAST-7

Sample ID	Distance from the Eutectic Isotherm (mm)	Velocity (um/s)	G_l (K/cm)	G_m (K/cm)
M7-2L-7	30	17.456	26.498	23.75
M7-2L-9	50	20.357	26.559	24.5
M7-3L-1	62.3	20	26.6	23.95
M7-3L-4	72.3	20	26.6	24
M7-4L-6	77.15	21.241	26.716	24.25
M7-4L-5	82.831	21.325	26.698	24
M7-4L-4	89.922	20.843	26.755	24
M7-4L-3	93.433	20.878	26.775	24
M7-4L-2	99.084	21.206	26.693	24.1
M7-4L-1	102.405	18.528	26.761	23.75
M7-5L-5	113.1	11.964	27.208	24.25
M7-5L-4	118.1	11.489	27.131	24
M7-5L-3	121.412	11.265	26.963	23.75
M7-5L-2	127.193	11.311		
M7-5L-1	131.2	11.068	26.36	24.3
M7-5L2-1	141.5	10.811	25.882	23.65
M7-5L2-2	146.321	10.23	26.135	23.6
M7-5L2-3	149.402	10.104	26.688	23.25
M7-5L2-4	156.083	11.808	27.371	23.4
M7-5L2-5	160.764	13.82	26.461	23.25
M7-5L2-6	165.7	17.985	23.869	23.25

Fig.13 shows MICAST-7 within the alumina crucible (a), when it is taken out from the crucible (b) and transverse microstructures on several transverse sections along the sample length, similar to MICAST-6 shown above. Alumina seems to have reacted and adhered to the sample surface at several locations. There are also several locations where the melt seems to have detached from the crucible wall resulting in radial depression, for example at 44.5 mm (Fig. 13(b)).

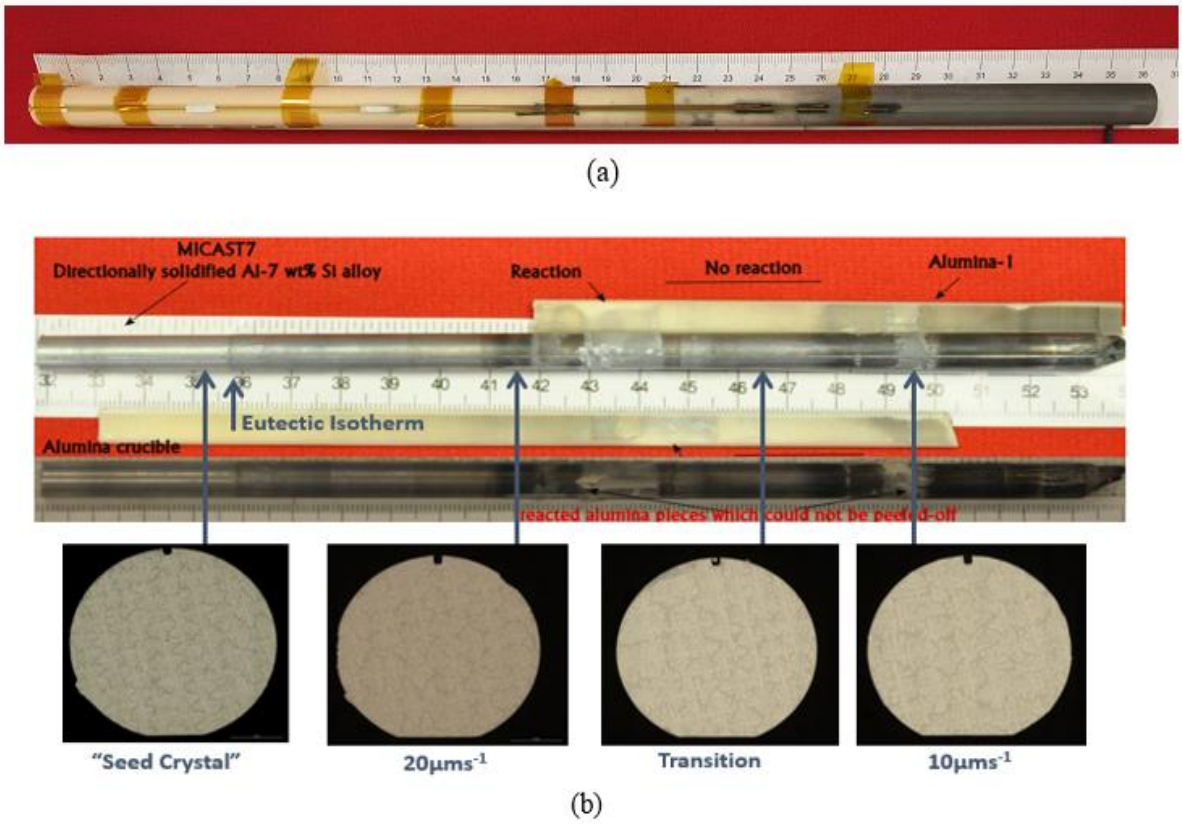

Figure 13 Solidified sample within the alumina crucible (a), and pulled out of the crucible and microstructures pointing towards the corresponding effects of external influence on the crucible (b). The 35.3 mm mark on the X-ray radiograph corresponds to the zero-mm mark for the montages

These detachments are clearly visible in the X-ray radiograph images of the MICAST-7 sample while it was still in the alumina crucible (Fig. 14). This figure includes longitudinal view of the sample after it was polished (Fig. 14 (c)), which shows that these surface depressions were 7-8 mm long. These surface depressions are clear evidence of liquid column getting detached from the crucible wall creating a liquid-vapor interface free to respond to the applied thermal gradient and cause Marangoni convection.

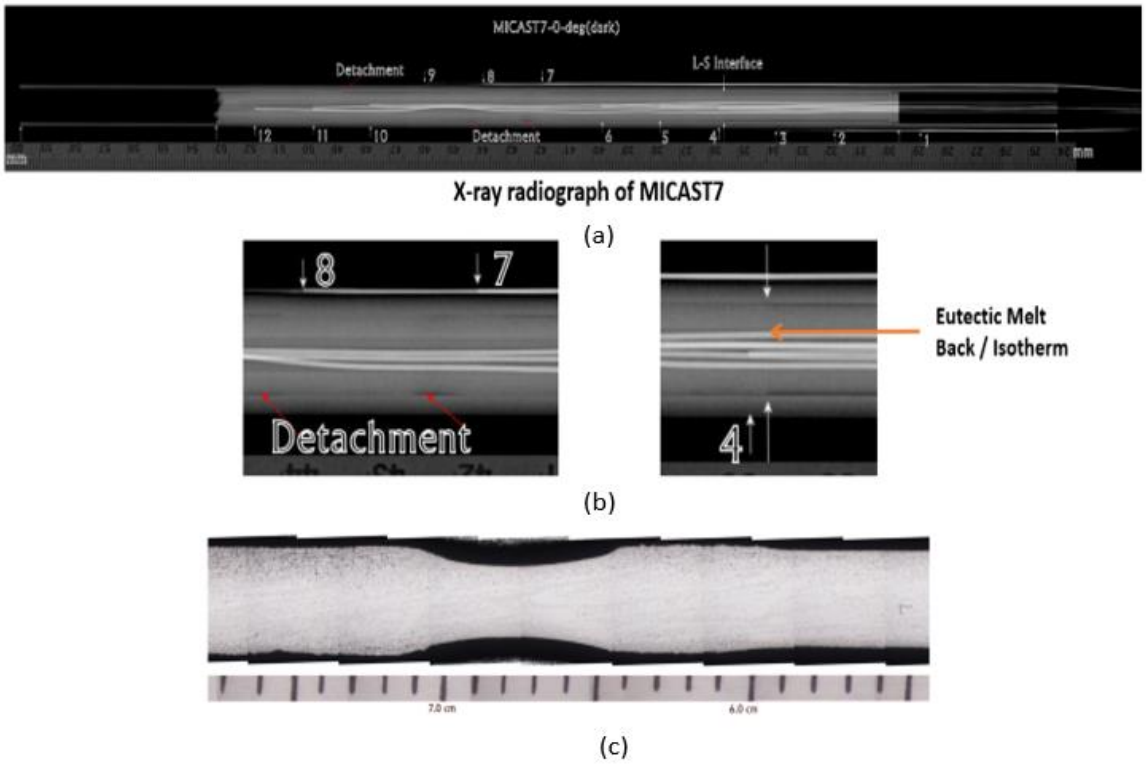

Figure 14 X-Ray radiograph of MICAST-7 sample, clearly identifying the surface voids and dislocations on the surface

In this sample, the growth speed was decreased from 20 μm/s to 10 μm/s at 84 mm from the eutectic isotherm.

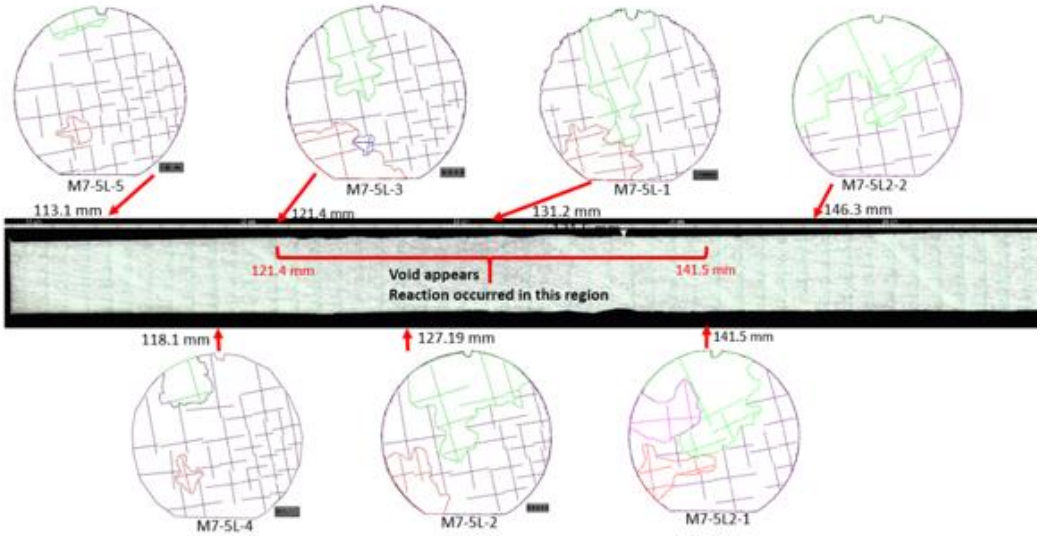

Figure 15 Results of image analysis on microstructures of MICAST-7

Fig.15 shows transverse views at several locations along the directional solidification length of the sample. Individual grains can be identified by their corresponding side-arm orientations. Several spurious grains can be seen to have formed in this sample where the primary dendrite alignment is very different from that in its seed portion.

4.1.3. MICAST-2-12

Table-3 lists locations of the transverse sections in MICAST-2-12 sample, and the corresponding growth speed and the thermal gradients at these locations. Fig.16 shows an X-ray radiograph of this sample. Melt-crucible detachment (dark features) is visible at three separate locations along the length of the directionally solidified sample. Figure 17 (a) shows a longitudinal view of this sample. The unmelted sample seed is at the left. The eutectic isotherm is the white looking vertical band at zero-cm mark. The mushy-zone would have been about 13-mm long and the rest would have been a column of liquid at the onset of directional solidification. There was about 1.1 cm long surface detachment in the melt column ahead of the mushy-zone. A grain with completely different orientation has apparently formed during subsequent DS. This grain has formed in the immediate vicinity of the ‘surface void’. Similar 2.5 mm long surface detachment was seen at about 53 mm (Fig. 17(b)). A misoriented dendrite is visible on the longitudinal section.

Table 4 Growth Conditions and Sample Location for MICAST-2-12

Sample ID	Distance from the Eutectic Isotherm (mm)	Velocity (um/s)	G_l (K/cm)	G_m (K/cm)
MICAST-2-12-T1	38	40	31	32
MICAST-2-12-T2	44.3	40	33.5	32.75
MICAST-2-12-T3	51	40	33	31.9
MICAST-2-12-T4	59	40	30.8	31.4
MICAST-2-12-T5	69	40	32.8	32
MICAST-2-12-T6	79	40	30.3	30.75
MICAST-2-12-T7	86	40	31	31
MICAST-2-12-T8	99.3	40	30.2	28.85

Figure 16 X-Ray radiograph of MICAST-2-12 sample and the directionally solidified MICAST-2-12 specimen

The sections following the surface void showed presence of spurious grains with orientation different than that of the seed.

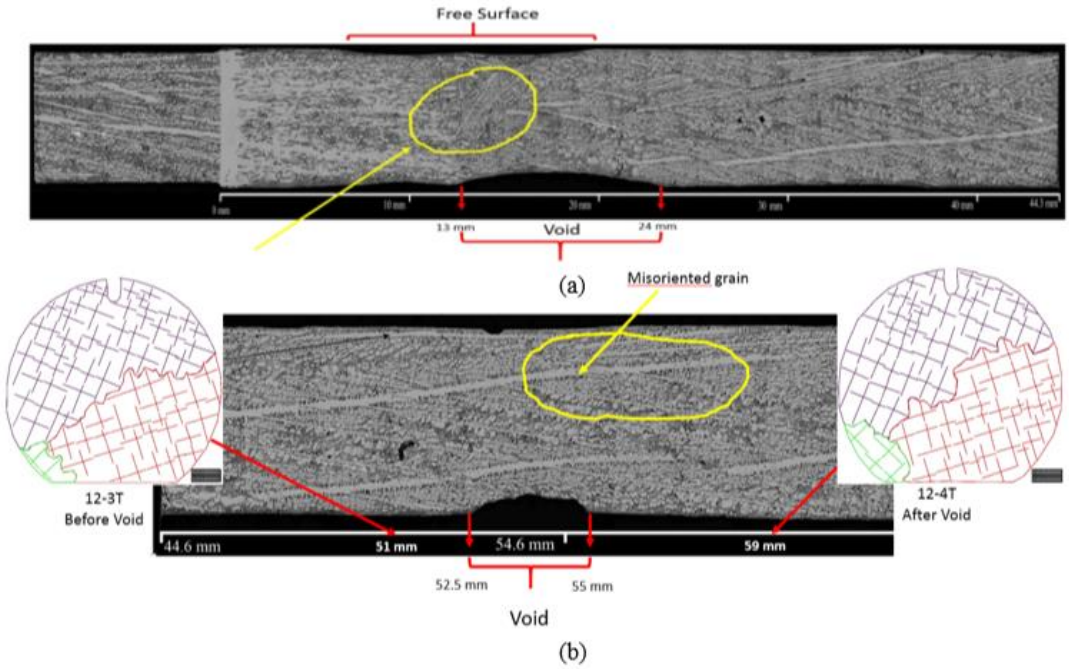

Figure 17 Result of image analysis on Microstructures of MICAST-2-12 sample exhibiting presence of spurious grain due to the presence of void

4.1.4. Electron Beam Scattered Diffraction (EBSD)

Electron Beam Scattered Diffraction (EBSD) has been successfully used for characterizing crystallographic orientations in microstructures for measuring misorientation, grain size, and crystallographic texture[42].

A typical EBSD analysis of MICAST-7 is shown in Fig. 18.

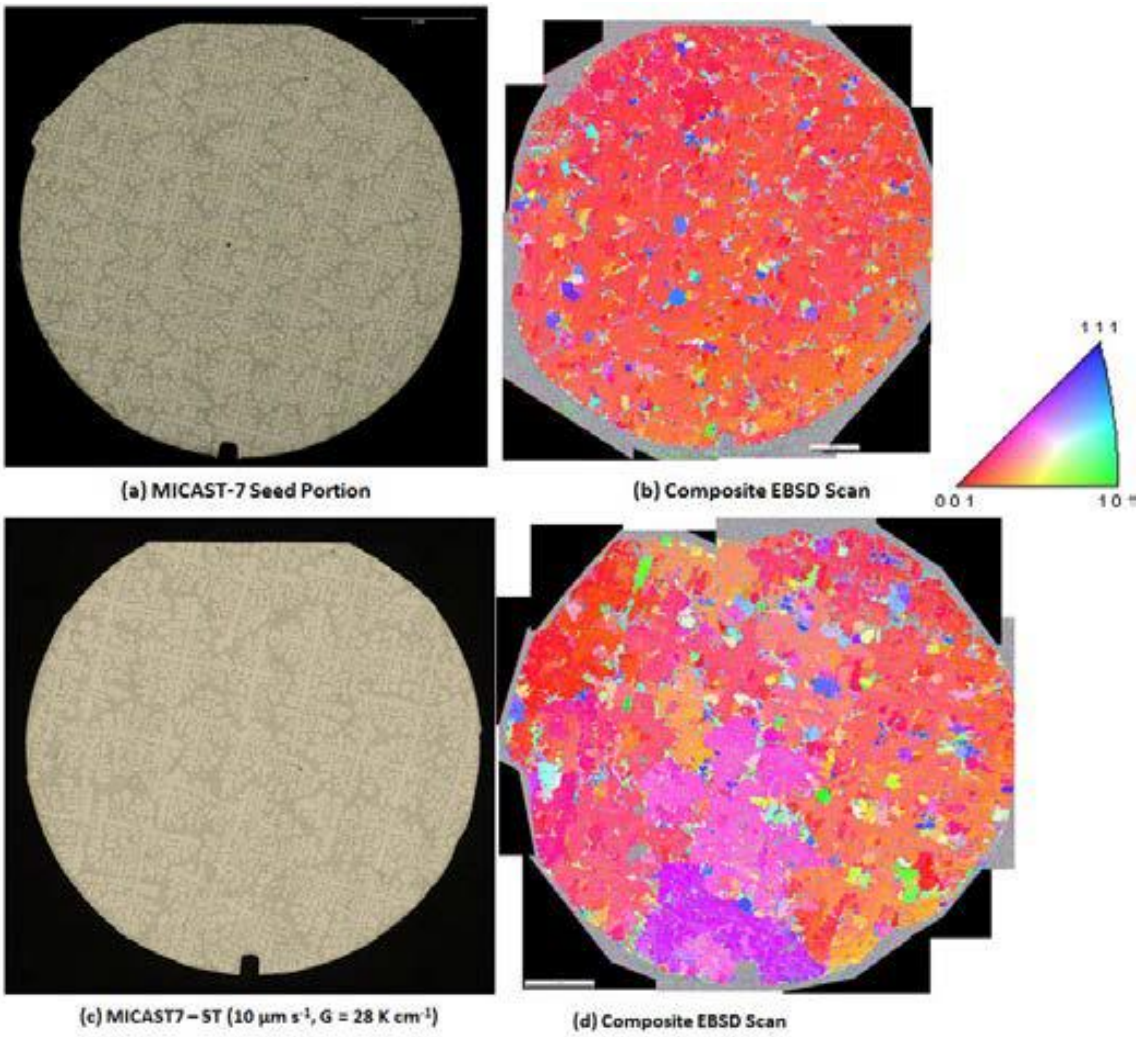

Figure 18 Comparison of primary dendrite alignments in the (a) seed portion and (c) in the portion which was DSed on the Space Station (MICAST-7, Al-7%Si, 10 μm s^{-1}). (b) and (d) are the corresponding Electron Beam Scattered Diffraction images based on the orientation map shown in the inset.

The inset shows the colors associated with various crystal orientations. Orientations along [001] appear red, those along [111] blue, and along [101] green in the EBSD images

of the transverse sections. MICAST-7 Seed portion (Fig 18 (a)) and its EBSD (Fig. 18(b)) show [100] orientation and no spurious grain on the entire sample cross section. However, MICAST 7-5T which is from a portion directionally solidified on the space station shows spurious grains and very poor dendritic alignment (Fig. 18(c)). The corresponding EBSD (Fig 18 (d)) shows several purple colored grains which corresponds to almost 45 degrees away from the original [100] orientation.

In summary, examination of an Al – 7wt. % Si alloy directionally solidified in the quiescent microgravity environment aboard the International Space Station revealed primary aluminum dendritic grains that significantly deviated from the expected <100> orientation. For terrestrially grown sample, the misorientation can be attributed to the convection due to the buoyant forces. However, spurious grains forming in the convection-free low gravity environment of Space Station is totally unexpected.

4.2. PFMI (SCN-0.24H_2O)

Images from PSI-PFMI 15 video[32] were extracted using Video to Picture: Aoao Photo Digital Studio software and image analysis was done using ImageJ. Fig. 19 (a) shows a portion of the PFMI-15 video where the ring-heater was present in the view keeping middle portion of the SCN-0.24H_2O sample melted. The heater was then translated to the left at 21:23:31 (Greenwich time) leading to cooling of the melt and staring solidification of preexisting grains from both the left and right side.

Since the heater was moved to left, the right dendritic array solidifies faster than the left. The tip velocities for both, right and left dendritic array were measured as a function of time and are plotted against time in Fig. 20. Since the heater was moved to the

left, the left portion of the melt remained warmer than the right side of the crucible after the heater withdrawal. The right dendritic array solidified faster than the left.

(a) (b)

Figure 19 (a) Heater moving out towards left and (b) Dendrites on right growing faster

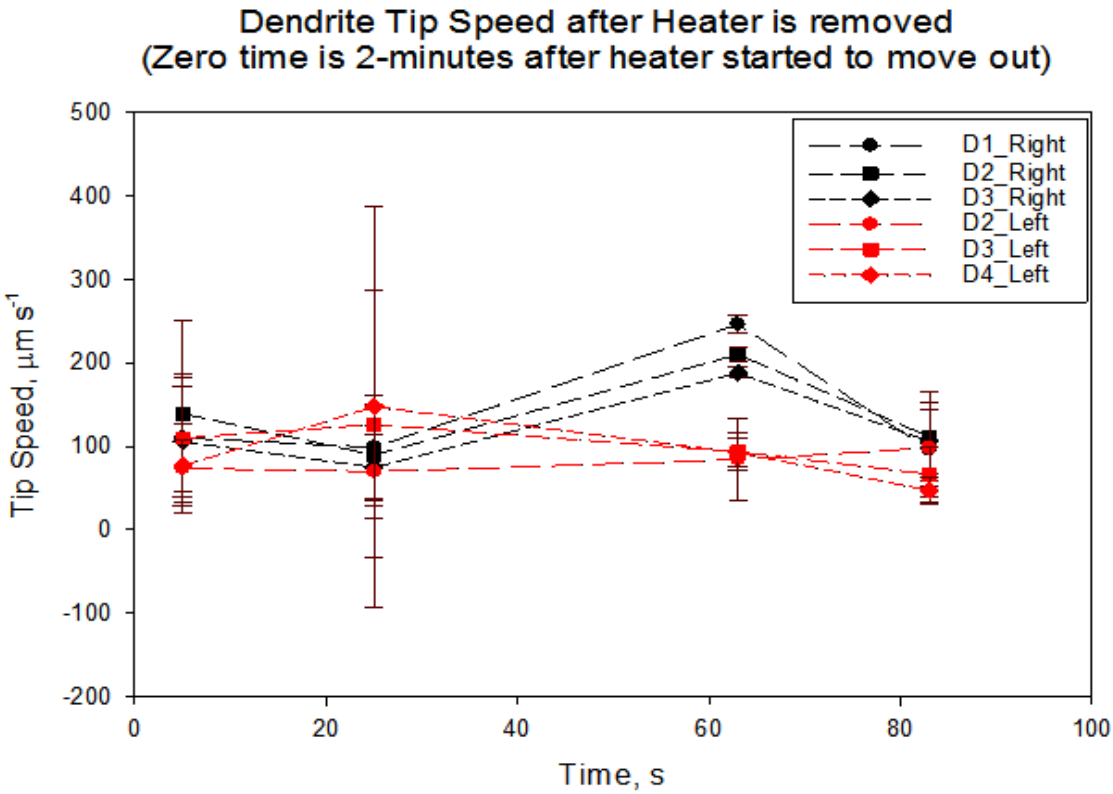

Figure 20 Dendritic tip speed plotted against time after heater is removed

Portion of the PFMI-videos[32] (PFMI-15, Position 46398 mm: SCN-0.24 wt% Water with N_2 added) from Time 21:14:50 onwards shows Marangoni Convection occurring in the vicinity of a gas bubble which is adhered to the inside wall of the quartz ampoule during DS on the Space Station (Fig. 21). Red circled object is the gas bubble adhered to the ampoule wall which is analogous to the voids seen in our MICAST experiments. In this video, tiny bubbles ('tracer bubbles') can be seen to follow a circular path, moving from the liquid column ahead into the mushy zone on the left side and then emerging from the mushy zone and rising up into the melt and then again coming down into the mushy-zone. The white marked path is a typical circular path followed by one of the tiny tracer bubble. We believe that this flow is caused by Marangoni convection because of the large (~ 3-mm diameter) bubble adhered to the ampoule in a positive thermal gradient. Since the melt is hotter on the right-hand side of the image, the liquid-vapor surface tension on the right side of the adhered bubble is lower as compared with the left side of the adhered bubble. This would make the fluid on the bubble surface move from the right side of the adhered bubble to its left side causing a Marangoni convection.

Figure 21 Circular path (marked in white) followed by tracer bubbles marking the Marangoni Convection field set up due to bubble adhered on the wall (marked in red)

For scale, the thermocouple wire at the bottom is 0.5 mm in diameter. Circulatory path of two tracer bubbles (called upper and lower tracer bubbles) was followed between 21:16:03 to 21:16:21 (GST) to measure the magnitude and velocity of the fluid flow along two typical isostream lines. These two tracer bubbles are shown in Fig. 22.

Figure 22 Upper and lower tracer bubble for measuring velocity

Fig. 23 shows the magnitude and direction of flow along the two circulating paths (the upper and lower tracer bubble) caused by the Marangoni flow. The arrows in Fig. 23 represent the magnitude and direction of the flow stream followed by the upper and the lower tracer bubbles respectively. The flow reaches as far as 3 mm into the bulk melt ahead of the dendritic array tips. The flow accelerates as it comes towards the tips of the dendrites (or towards the adhered 3-mm diameter bubble below) and decelerates going back up again. The fluid speed while going towards the array tips is larger than that while returning back.

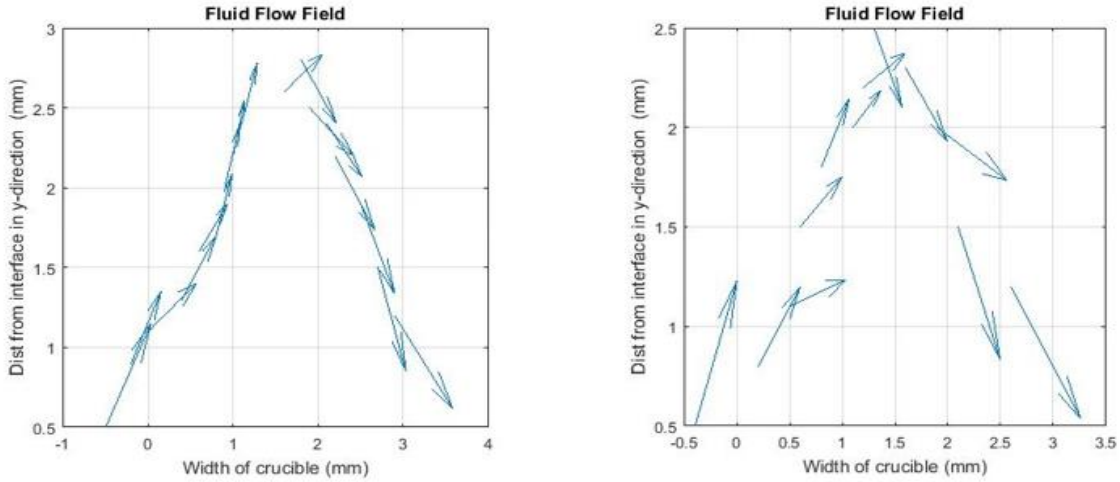

(a) (b)

Figure 23 Fluid flow Stream (a) Upper Tracer Bubble (b) Lower Tracer Bubble

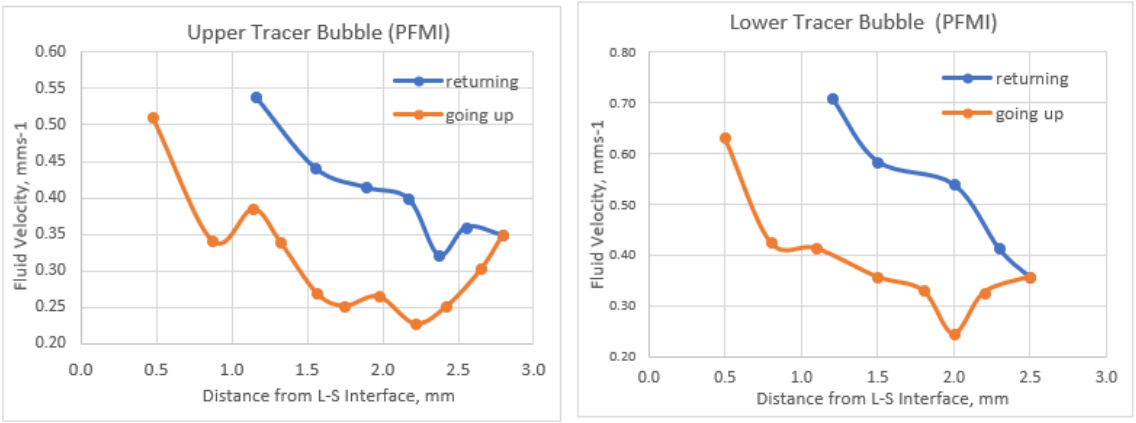

(a) (b)

Figure 24 Variation of Fluid Velocity with Distance from L-S interface (a) Upper Tracer Bubble (b) Lower Tracer Bubble

Fig. 24 plots the variation in the fluid velocity traced by using the upper and lower tracer bubbles as a function of distance from the dendritic array tips. The orange lines indicate the decelerating flow speed as the flow moves away from the dendrite array tips towards the bulk melt. The blue lines indicate- that the fluid speed increases as the tracer bubbles approach the adhered bubble located just below the dendrite array tips. For same distance away from the dendrite array tips, the fluid velocity is higher while coming

towards the arrays and keeps on decreasing as it moves back into the bulk melt ahead away from the arrays.

Since the above observations are made based on the image analysis and measurements using the images extracted from the video, a simulation using COMSOL software for directional solidification of SCN-0.24H_2O alloy would help in demonstrating the results better and can be useful for comparing it with our proposed work on Al-7Si alloy.

4.3. COMSOL Simulation

COMSOL Multiphysics software is useful for carrying out 2D and 3D simulations for various fluid flow applications[43, 44]. It consists of numerous physics modules which have almost all equations governing the fluid flows. It takes into consideration the boundary conditions, thermophysical properties of the melt and allows the user to input customized equations as per the requirement. In this work, COMSOL has been used for carrying out a 2D simulation of the DS of SCN-0.24H_2O and Al-7Si alloy.

4.3.1. Simulation: PFMI (SCN-0.24H_2O)

4.3.1.1. Assumptions.

1. 2D geometry is considered. The crucible is considered rectangular.
2. Symmetry is assumed. Half of width of the crucible is considered for simulation.
3. A 1.3 mm diameter void is placed such that part of it (1mm) is within the mushy zone (similar to the PFMI-15 video described above).
4. Linear Temperature profile is considered on the walls except on the free surface.

$T = T_0 + (Y*G_L)$ where T_0: Reference Temperature (K), T: Temperature at Distance Y (K),

Y: Distance from the bottom of the mushy zone (m), G_L: Liquid Thermal Gradient (K/m)

4.3.1.2. Boundary conditions.

1. No slip condition is imposed on all walls except the free surface. U=0.
2. Slip condition is imposed on void. $[\mu(\nabla\vec{u} + (\nabla\vec{u})^T)].\vec{n} = \Upsilon\nabla_t T$

This accounts for convection due to thermal gradient across the void.

Mushy zone is a mixture of solidifying dendrites and interdendritic liquid. It has been treated as a porous medium. Even though mushy-zone extends from the liquidus (329.14 K) down to the eutectic temperature (292 K). Only the top 4.4 mm of the mushy-zone has to be considered permeable (Fig. 25).

Domain size: Length: 21.3 mm, Width: 5 mm

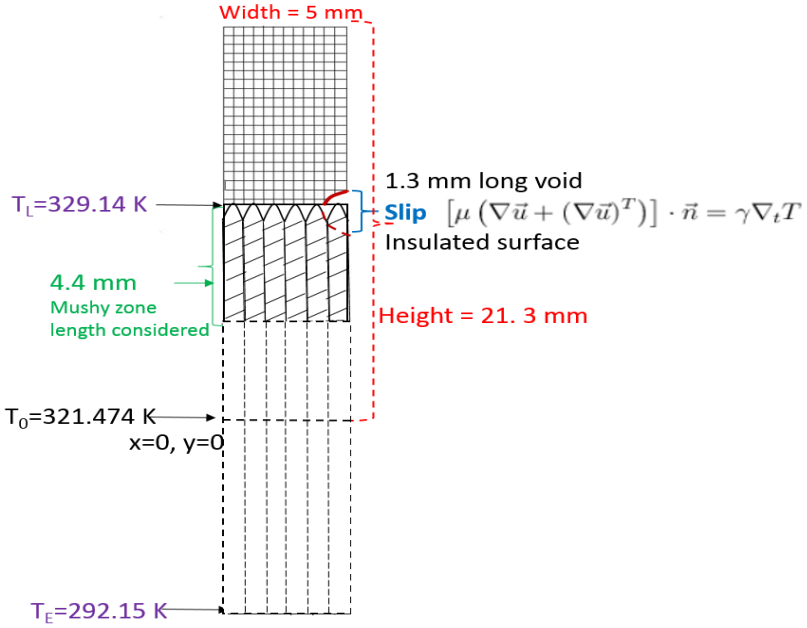

Figure 25 Domain with Boundary Conditions

Using above domain, two-dimensional simulation of Directional solidification of SCN-0.24H_2O is carried out.

4.3.1.3. Physics used. Darcy's law is generally used to examine the fluid flow behavior in packed porous beds[45]. It is analogous to Fick's law of diffusion in mass transport, and it does not account for the viscous forces arising out of the free media flow. For cases involving porous media where the viscous forces could play a significant role depending on the pore geometry, distribution in the media and the fluid properties, Darcy's law falls short and must be replaced with a stronger equation that considers the momentum transport due to viscous effects and the pressure gradient arising from the shear effects in pore channel as well. Under such situation, Brinkman equation which is an extension of Darcy's law and assumes laminar flow, is used. For processes in which turbulence also contributes, an additional term that accounts for the inertial effect is introduced.

The system considers stationary, incompressible, laminar flow in free channel. Navier Stokes equation is solved to get the fluid velocity profile.

$$\rho(\mathrm{u}.\nabla)\mathrm{u} = \nabla.[-\mathrm{pI} + \mu(\nabla\mathrm{u} + (\nabla\mathrm{u})^T)] + \mathrm{F} \quad [6]$$

$$\rho\nabla.(\mathrm{u}) = 0 \quad [7]$$

where μ denotes the dynamic viscosity (Pa·s), u refers to the velocity in the open channel (m/s), ρ is the fluid's density (kg/m^3), and p is the pressure (Pa).

For the porous domain, the Brinkman equations with Forchheimer correction is used to describe the flow:

$$\frac{\mu}{\kappa}\mathrm{u} = \nabla.[-\mathrm{pI} + \frac{\mu}{\varepsilon_p}(\nabla\mathrm{u} + (\nabla\mathrm{u})^T)] - \frac{\rho\varepsilon_p c_f}{\sqrt{k}}u|u| \quad [8]$$

κ denotes the permeability of the porous medium (m^2), ε_p is the porosity (dimensionless), and the dimensionless friction coefficient is $C_f = \frac{1.75}{\sqrt{150\varepsilon_p^3}}$. [45]

The terms on the left-hand side of the Navier-Stokes equation denotes momentum transferred by convection in free flow. The Brinkman equation makes use of the contribution due to the drag force experienced by the fluid flowing through a porous medium. The last term in the right-hand side of Equation 7 is the Forchheimer correction[46], β for turbulent drag contributions.

$$\beta_f = \frac{\rho \varepsilon_p c_f}{\sqrt{k}}$$

Boundary conditions: u = 0 Wall: no slip

p = 0; $\mu(\nabla u + (\nabla u)^T) = 0$ Outlet: Pressure, no viscous stress

where the pressure level at the outlet is used as a reference value. Here, an extension of Darcy's flow is applicable, which is termed as Forchheimer Drag.

4.3.1.4. Parameters. Table 5 lists the thermophysical properties of the alloy used in PFMI experiments i.e. SCN-0.24H_2O. This properties were used for COMSOL simulation.

Table 5 Thermophysical Properties used for COMSOL Simulation

Term	Value	Unit	Parameter	Reference
G	716	K/m	Thermal Gradient	This work
R	5.00E-06	m/s	Growth speed	40
T_m	331.39	K	Melting point	31
T_l	329.35	K	Liquidus Temperature	53
T_e	292.15	K	Eutectic Temperature	53
C_p	2000	J/kg.K	Heat capacity	31
m_l	-200		Liquidus slope	53
D	1.16E-07	m^2/s	Diffusivity	31
K	0.222	W/m.K	Thermal conductivity	31

Table 5 Continued

Term	Value	Unit	Parameter	Reference
Υ	-8.20E-05	N/m.K	Temperature derivative of the surface tension	40
Λ	0.00035	m	Primary Dendrite Arm Spacing	40
K	0.0001		Partition coefficient	53

Physical Properties

The viscosity in mPAs of the alloy has been assumed to be same as pure SCN,

$$\mu = 4.11 - 0.0263\ T^{47} \qquad [9]$$

Temperature dependence of the melt density (g/cm^3) has been assumed to be same as that of pure SCN.

$$\rho = -7.849 \times 10^{-4}\ T + 1.0323^{48} \qquad [10]$$

Fig.26 shows the SCN-0.24H_2O phase diagram[49]. SCN-0.24 wt. pct. H_2O is equivalent to SCN-0.0103 mole fraction H_2O.

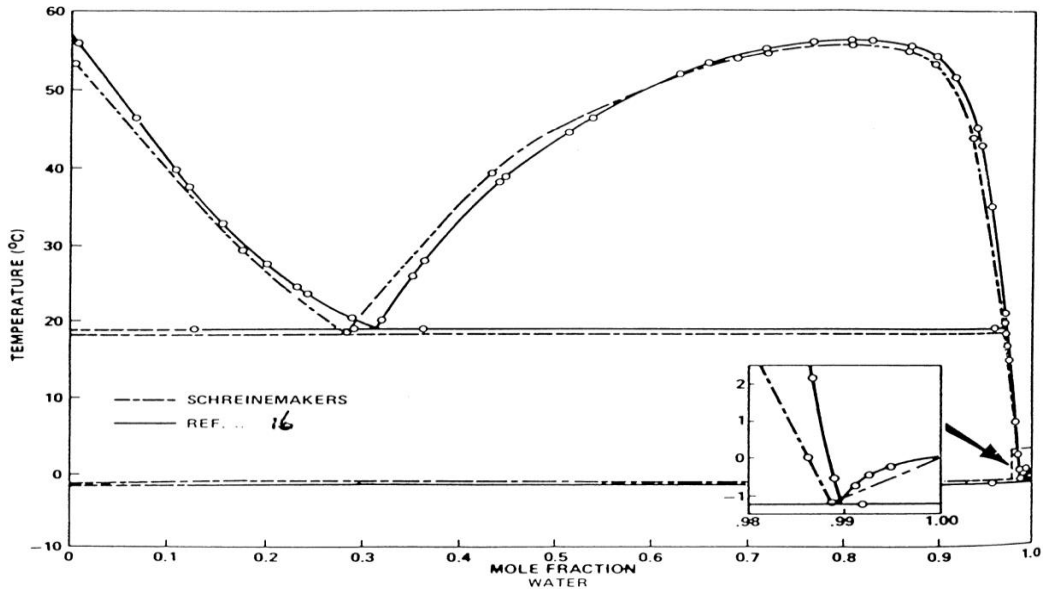

Figure 26 Phase diagram for SCN-0.24H_2O with water in terms of mole fraction

As shown in the SCN-0.24H_2O phase diagram given in Fig, 26, the solute partition coefficient *k*, is defined as the ratio of the solid and the liquid compositions in equilibrium which is assumed to be 0.0001.

Mushy Zone Permeability

The porosity, ε_p of the mushy zone has been treated same as the fraction liquid, f_L, in the Scheil Equation[50]

$$f_L = \left[1 - \left(1 - \frac{(Tm - Tl)}{(Tm - T)}\right)^{\frac{1}{1-k}}\right] \quad [11]$$

where, *Tm*: Melting Point of the alloy (K), *Tl*: Liquidus Temperature of the alloy (K), *T*: Any temperature where Fraction liquid is measured (K), *k*: Partition Coefficient

Using the Scheil equation, the variation of fraction liquid with temperature is plotted in Fig.27:

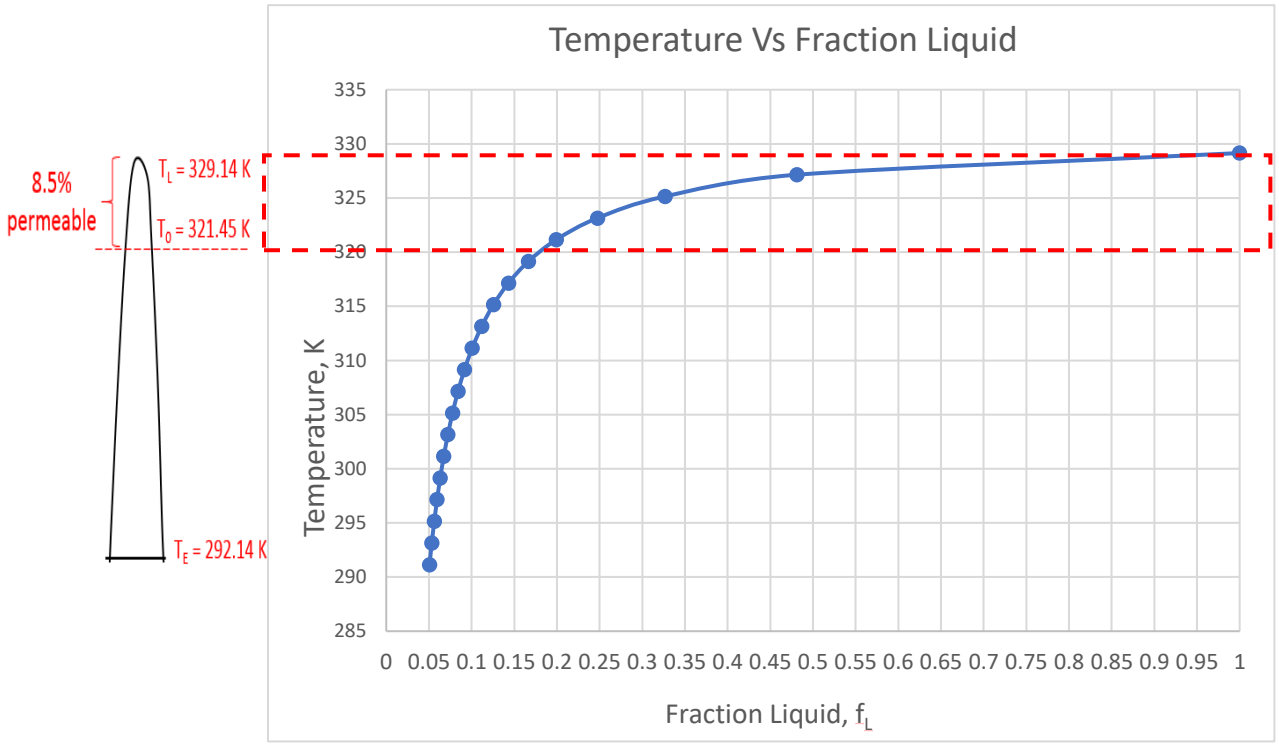

Figure 27 Variation of Porosity with Temperature

It shows that the fraction liquid (mushy zone porosity) drops to about 20% at 321.45 K. Therefore, the rest of the porous region below 321.45 K has been assumed to have zero permeability.

Mushy Zone length = $T_L - T_E / G_L$ = (329.14 – 292.15) / 7.16 = 5.16 cm. However, only 0.44 cm of the mushy-zone near the array tips [$(T_L - T_0)/ G_L$ = (329.14 – 321.45) / 7.16 = 0.44 cm] has been permeable.

Based on previous work on porous media, the permeability can be determined using the below Kozney–Carman permeability equation[51],

$$\kappa = \frac{\varphi^3}{4.2\, S_v^2 (1-\varphi)^2} \quad [12]$$

where φ: Fraction interdendritic liquid, *Sv*: Dendrite specific surface area (*Sv*) in the quenched mushy zone of directionally solidified alloys,

$$Sv = \lambda^{-1} S^{*-0.33}(3.38 - 3.29\varphi + 8.85\varphi^2)\ ^{52} \quad [13]$$

where λ: primary dendrite spacing, and S^* is the extent of side branching,

$$S^* = D_l\, G_{eff} / [V m_l\, C_o\, (k - 1)/k] \quad [14]$$

where D_l being solutal diffusivity in the melt, G_{eff}, the effective thermal gradient, V, the growth speed, m_l, the liquidus slope, Co, the solute content of the melt, and k the solute partition coefficient.

4.3.1.5. PFMI simulation results. Fig. 28 shows the fluid isostream contour lines from COMSOL simulation of PFMI experiment. The large red arrow is indicative of the maximum fluid velocity. A 1.3mm diameter bubble sets up a thermocapillary field that extends to approximately three diameters upstream into the liquid, with the flow speeds being most forceful at the interface. The fluid velocity is higher near the L-S interface close to the void.

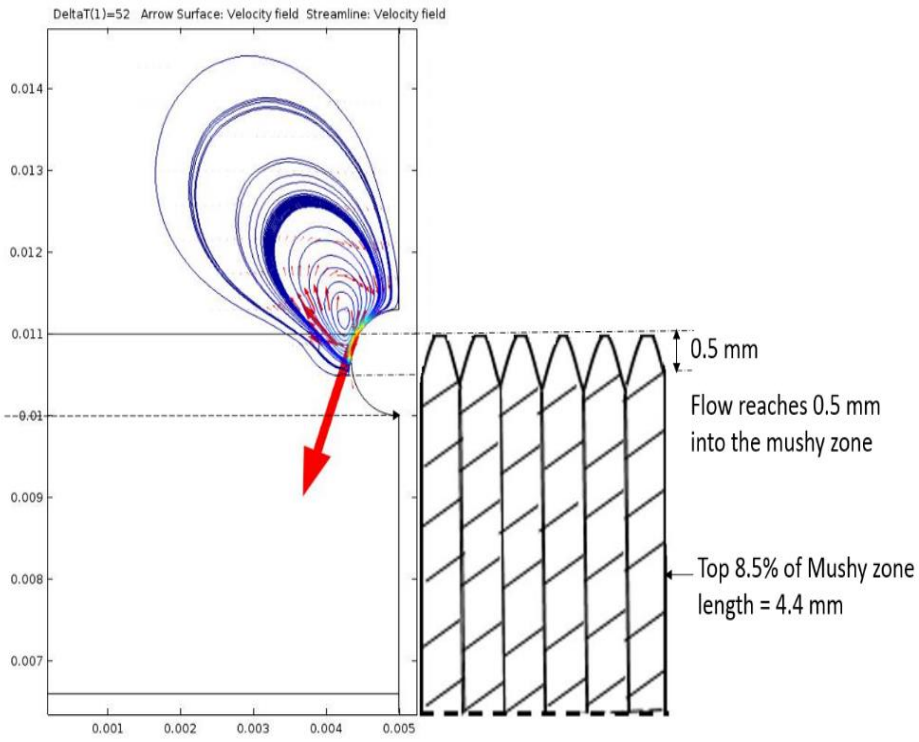

Figure 28 Velocity Field with Streamlines-SCN-0.24H_2O

The fluid decelerates as it moves away from the array tips into the bulk liquid melt. This pattern is similar to that obtained using data from the PFMI experiments. In actual PFMI experiments, we used tiny tracer bubbles to track the fluid flow field, here in the simulation the streamlines are considered to be the path traced by massless, particles. For plotting the data shown in Fig. 29, two streamlines are selected based on the maximum distance they achieve from the L-S interface while moving into the bulk melt. For instance, streamline#14 is similar to the upper tracer bubble in the PFMI experiment as both reach ~3mm away from the L-S interface into the bulk liquid. Likewise, the streamline #11 is similar to the lower tracer bubble which travelled about 2.5 mm away from the array tips into the overlying melt pool.

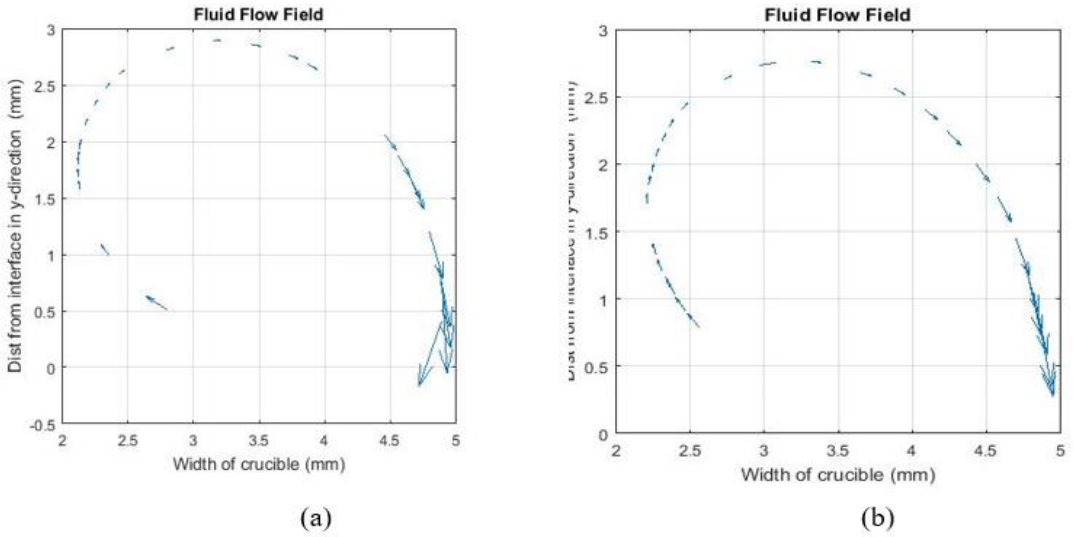

Figure 29 Flow field of (a) Upper Tracer Bubble (Streamline 14) (b) Lower Tracer Bubble (Streamline 11)

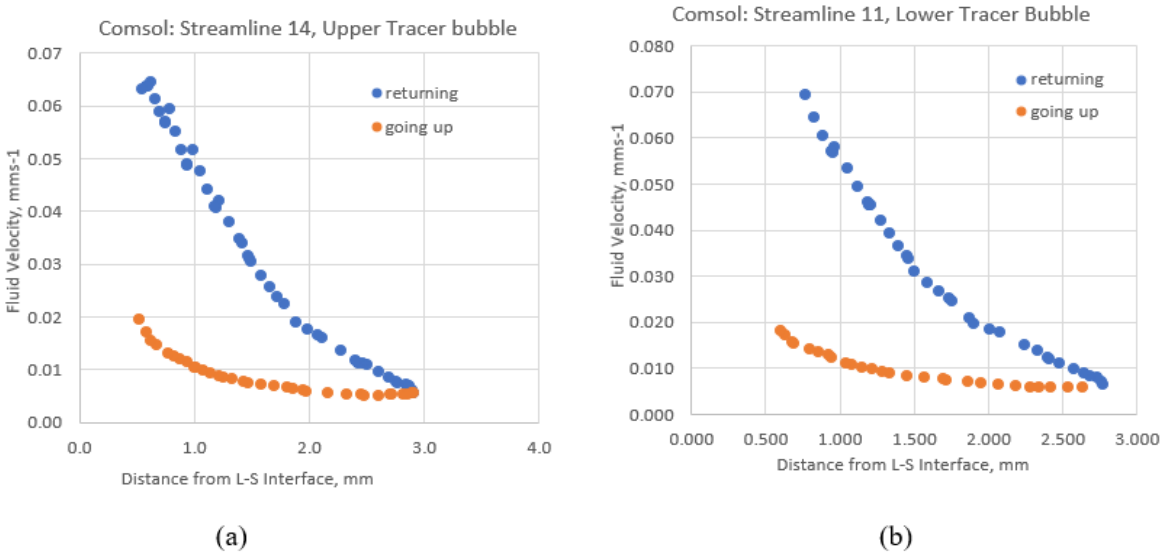

Figure 30 Fluid Velocity vs Distance from L-S interface (a) Upper Tracer Bubble (Streamline 14) and (b) Lower Tracer Bubble (Streamline 11)

Figure 30 plots the COMSOL simulation data extracted from the streamline 14, which simulates a flow line going up same distance as the upper tracer bubble of the PFMI experiment, and those extracted from the streamline 11, which simulates a flow path similar to the lower tracer bubble of the PFMI experiment. There is a qualitative agreement between the COMSOL simulation and the PFMI experiments.

However, the experimentally observed flow speeds measured from the PFMI-15 video (Fig. 24(a) and (b)) are almost one order of magnitude less than those indicated from the COMSOL simulation (Fig. 30 (a) and (b)). It may be because the plots using PFMI data were based on velocity measurements of tiny tracer bubbles and not massless particles as in the COMSOL simulation. There may be four reasons for this disparity.

- The PFMI experiments involve a three-dimensional interaction between the alloy melt, dendritic array and the nitrogen bubble adhered to the crucible wall whereas our COMSOL simulation is two-dimensional.
- The alloy physical properties used for the simulations are based on assuming that the SCN-0.24H_2O alloy has the same properties as pure succinonitrile.
- It is well-known that the tracer bubble, no matter how tiny, will migrate up the thermal gradient because of the surface tension driven forces even in the absence of an adhered large nitrogen bubble. There the fluid stream lines measured from the PFMI experiments would have both components, one due to the Marangoni convection caused by the adhered 1.3 mm diameter bubble, and also the inherent migration of the tiny tracer bubble in response to the thermal gradient existing in the melt.
- During simulations, the stream lines can be followed from the bulk melt ahead into the mushy-zone near array tips and therefore data along the entire isostream lines are used, whereas for the actual experiments (PFMI-videos) it is only possible to extract data from portions of the flow lines which are above the array tips, not from those which are in the mushy-zone below the array tips.

The COMSOL simulation shows a flow pattern similar to the PFMI experiments (accelerating during moving downward towards the void or dendritic tip and having lower speed during return). The flow velocity spikes at the bubble-solid interface.

Fig. 31 compares the average speed along several flow contour lines reaching various distances from the array tips obtained from the experiments (PFMI video data from following recirculating paths of several tiny tracer bubbles) and those obtained from the COMSOL simulation. It shows a good qualitative agreement between the trend observed experimentally and that simulated by using COMSOL. However, the quantitative agreement is poor.

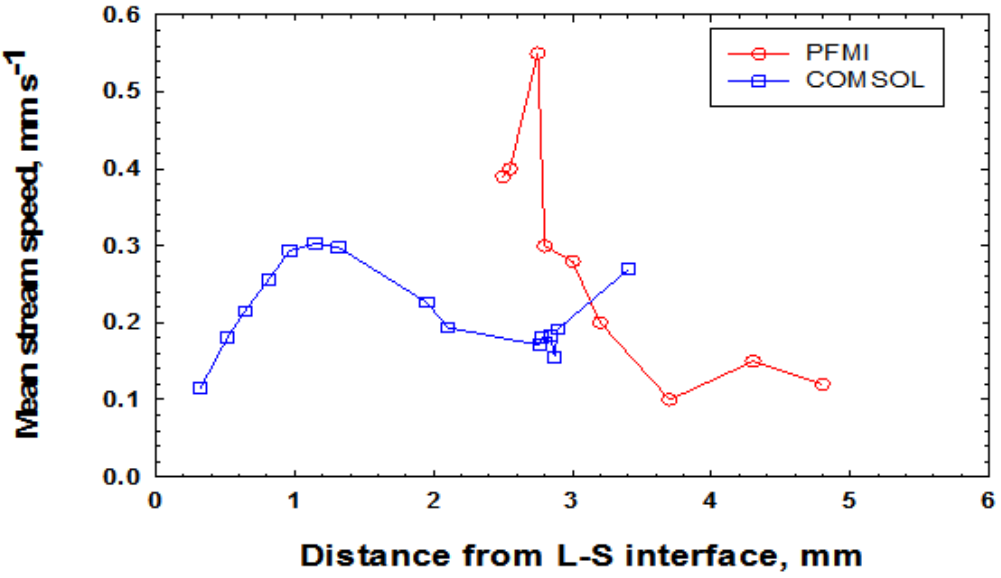

Figure 31 Variation of Mean Stream Speed with Distance from L-S Interface

4.3.2. Rotation of Dendritic Arms

There is also an evidence in PFMI video (Time: 21:14:32) of dendrite fragmentation and rotation in response to Marangoni convection caused by a bubble adhered to the ampoule wall. Fig. 32 contains three views extracted from the PFMI-15 video from a location where the preexisting dendritic array was being slowly remelted by

bringing the ring heater in the view (the heater was on the right side of these extracted still images) in the presence of a nitrogen bubble adhered to the crucible wall. The dotted line in Fig. 32 corresponds to the contours of the adhered bubble. A side arm (marked red) detaches from the primary dendrite trunk and then it begins to fall and rotate in response to the Marangoni flow even in the absence of gravity. The clock-wise rotation of this side arm was followed as a function of time by using time-lapsed images from the PFMI-video in order to measure the rotation of this fragmented side arm. The result is shown in Fig. 33.

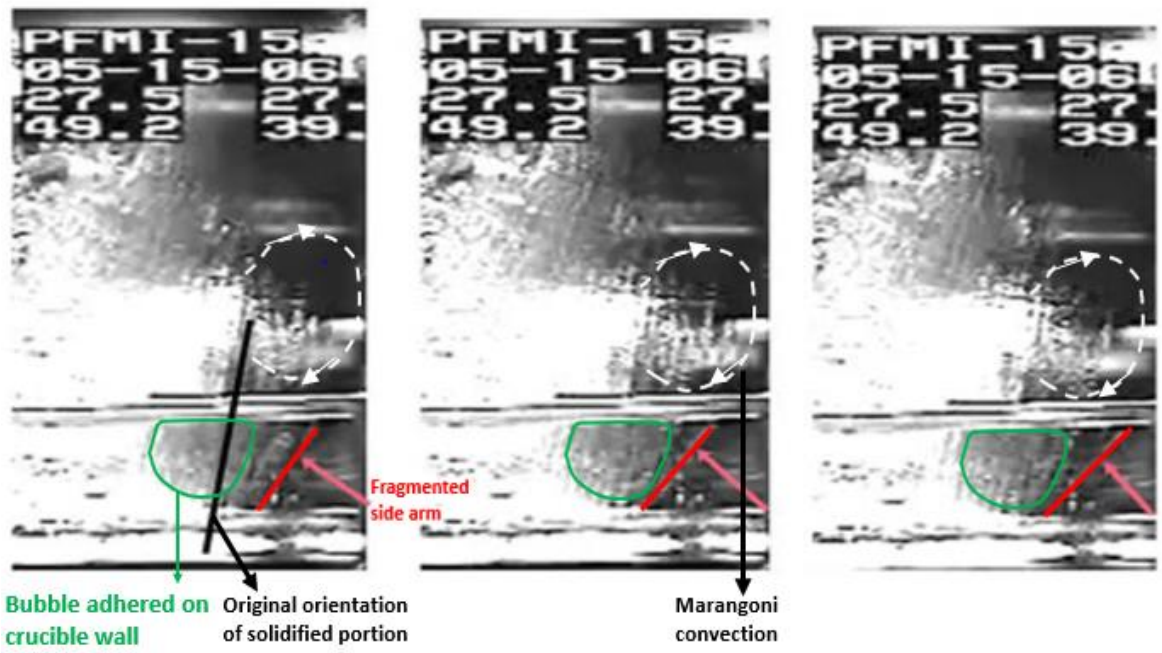

Figure 32 Rotation of Dendritic Side Branch in response to Marangoni Convection

Growth speed of the solidifying array ~5 μm s^{-1}, fluid speed obtained from COMSOL simulation ~0.5 mm s^{-1}. During 4.5 mm of DS, a fluid stream traverse 100 cycles➔ enough to fragment and rotate a side-arm!!

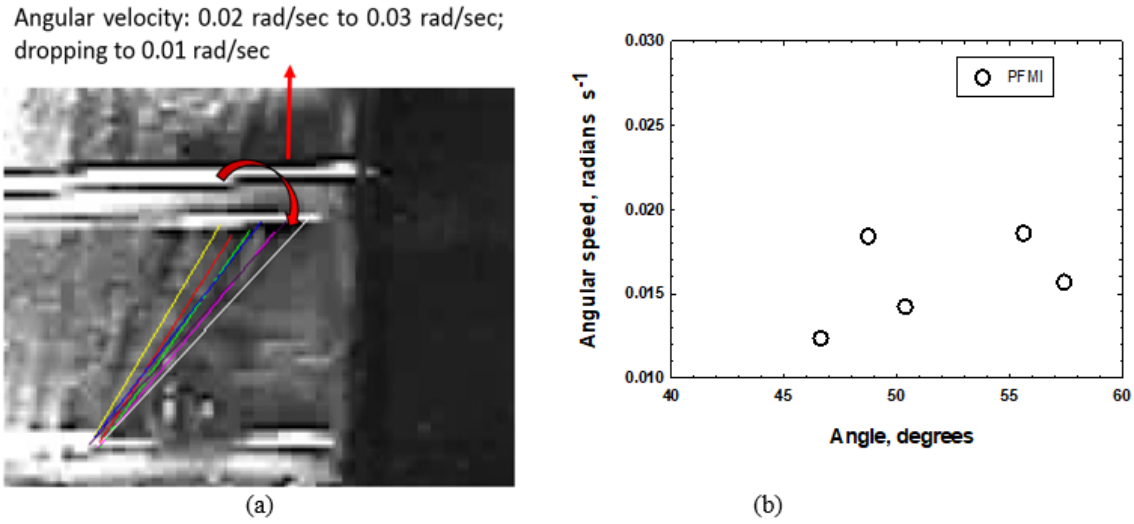

Figure 33 (a) Motion of the detached dendritic arm in response to the fluid flow; (b) Variation of Angular speed of dendritic arm with respect to dendritic orientation

The detached arm moves in clockwise direction, this was the path as observed by following the circular path of tiny tracer bubbles. In the absence of gravity, even if the arm got detached during the remelting of directionally solidified sample, it should have remained motionless. The video shows clear evidence of rotation of these broken side-arm fragments exactly in the manner earlier hypothesized in Fig. 4. The repeated impacts from the Marangoni convection induced flow lines would also be expected to cause such a clock-wise rotation. Let us recall that the speed of the flow incoming towards the fragmented arm on its right side is less than the speed as it moves further down wards (as indicated by PFMI simulations and also observed by following the tiny tracer bubbles in PFMI videos). The flow hits the right side of the fragmented side-arm downwards. And, then when the fluid emerges from the mushy-zone and begins to move back away into the bulk melt, it again hits the broken fragment on its left side in upward direction. This repeated impact apparently causes the fragment to rotate in the clock-wise direction.

It is interesting to note that for a typical growth speed of 5 μm s^{-1}, a recirculating flow having a mean speed of 0.5 mm s^{-1} would traverse the typical 4.5 mm long permeable region of the mushy-zone about 100 cycles before this portion of the mushy zone solidifies. 100 repeated cycles of the fluid impact on the right and left side of a side-arm is sufficient to break and rotate it by almost 45 degrees.

Once the dendrite fragment comes to rest, its final crystallographic orientation will be very different from the parent array. Subsequent growth of this misoriented fragment would lead to the formation of spurious grain even in the absence of gravity or gravity induced thermosolual convection.

4.3.3. Simulation: MICAST2-12 Experiment (Al-7Si)

4.3.3.1. Domain, boundary conditions and parameters.

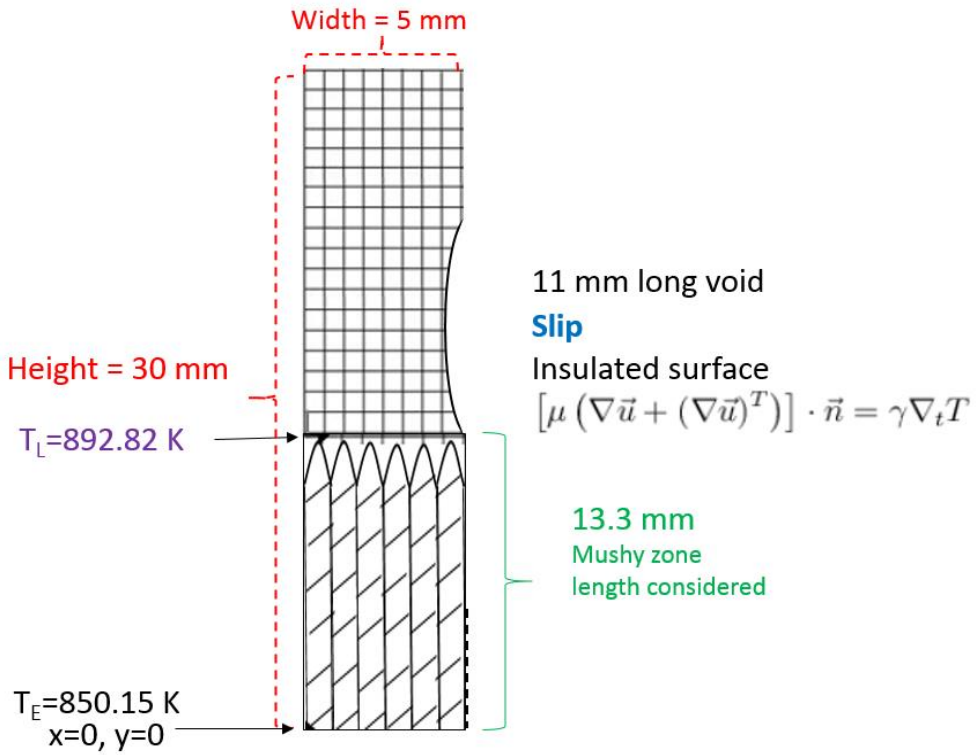

Figure 34 Domain used for COMSOL simulation of Al-7Si alloy: MICAST-2-12 with boundary conditions

Fig. 34 shows the boundary conditions used to simulate MICAST-2-12 experiment (Fig. 17(a)). Domain Size: Height: 30 mm, Width: 5 mm. All assumptions and boundary conditions are similar to SCN-0.24H_2O simulation. Porosity and permeability are calculated using the same equations (8), (9) as that in SCN-0.24H_2O case. Semi-circular void of 11 mm same as observed in MICAST-2-12 sample (Fig. 17(a)) is considered just above the dendritic tip. The Al-Si phase diagram given in Fig. 35.

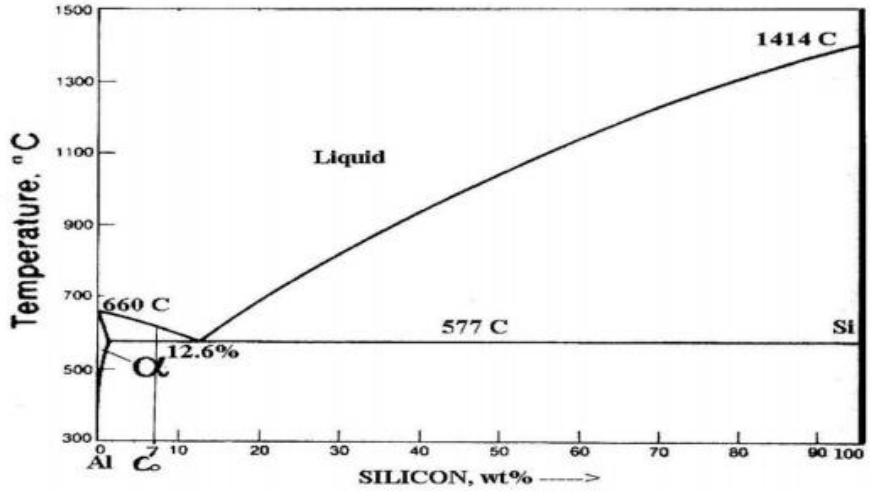

Figure 35 Phase Diagram for Al-7Si alloy[35]

The mushy Zone length is (T_L – T_E/ $G_{L)}$ = (892.82 – 850.15) / 32 = 1.33 cm. However, only the top 15% of the mushy zone is considered permeable.

Density dependence of Al-7Si on temperature[53] is given by:

$$\rho\ (g/cm^3) = 2.42 - 2.87 \times 10^{-4}\ (T - T_L) \qquad [15]$$

Similarly, the viscosity dependence on temperature[53] is given by:

$$\mu\ (mPa.s) = 0.206 \exp \frac{13385}{T} \qquad [16]$$

Using the Scheil equation (8), the variation of fraction liquid with temperature is plotted in Fig. 36.

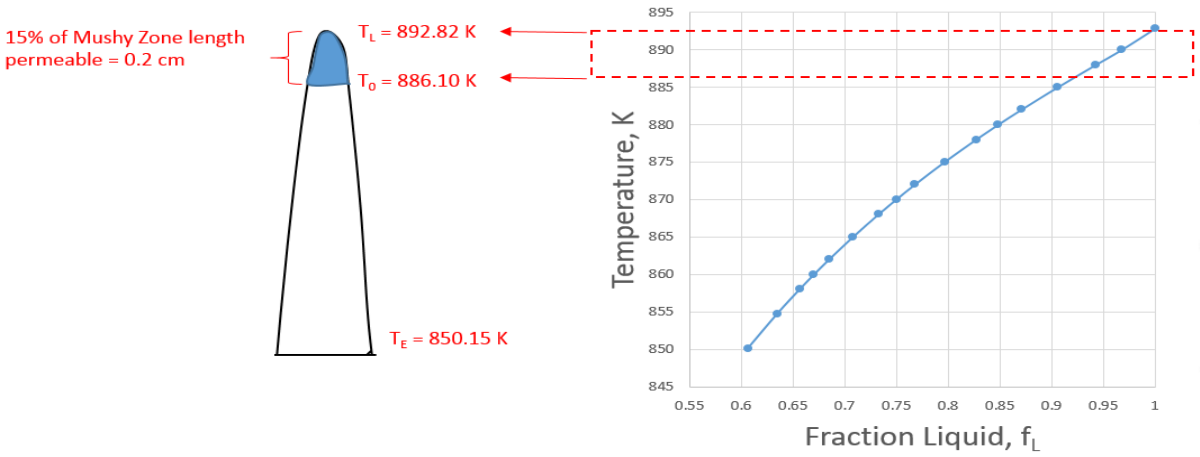

Figure 36 Variation of Porosity with Temperature for Al-7Si

4.3.3.2. *MICAST-2-12 simulation results.* Fig. 37 shows the velocity flow field caused by the Marangoni convection because of the surface pore on the right side. A comparison with the COMSOL simulation result earlier presented for SCN-0.24H_2O case (Fig. 28), shows that the fluid streams reach much higher i.e. traverses distance of ~12 mm above the array tips in case of the Al-7Si alloy as compared with distance of ~3mm in case of SCN-0.24H_2O. This indicates a much stronger convection during directional solidification of this region of the MICAST2-12 sample.

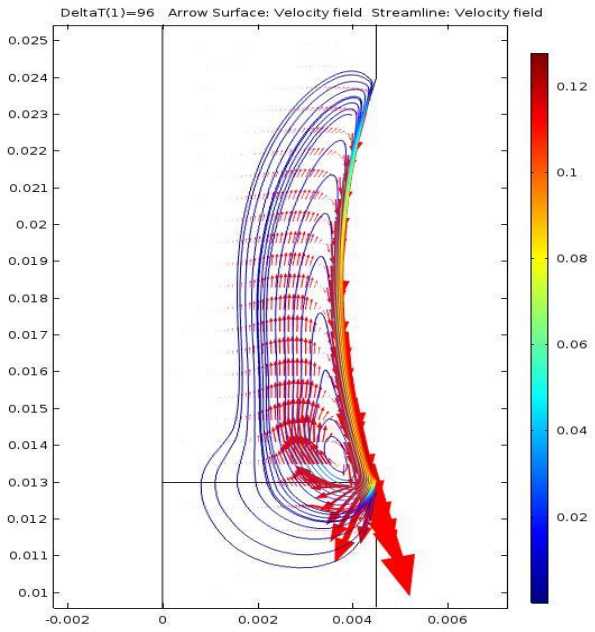

Figure 37 Velocity Field with Streamlines: MICAST-2-12 (Al-7Si)

Fig. 38 shows the COMSOL simulated fluid speed along a typical recirculating streamline. Zero on the x-axis corresponds to the mushy-zone tip, the positive distances are into the bulk melt ahead of the array and negative distances represent into the permeable portion of the mushy-zone below the array tips.

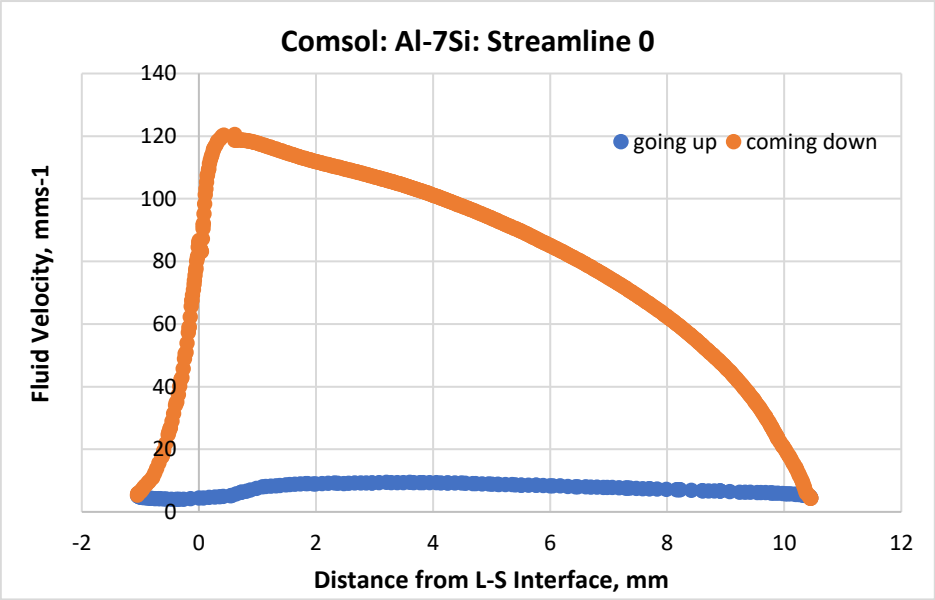

Figure 38 Variation of Fluid Velocity with Distance from L-S interface for Streamline 0

The flow travels into the mushy zone below the array tips by as much as 2mm. The speed of the flow near the array tips and even in the mushy-zone near the array tips is higher than in the bulk melt. At the same distance from the array tips, the fluid speed is higher as it comes towards the array than it is when it returns back from the mushy zone and traverses back into the overlying bulk melt. This trend is similar to that earlier observed in the SCN-0.24H_2O alloy during PFMI experiments: the recirculating Marangoni flow accelerates as it approaches the L-S interface and decelerates as it comes back into the bulk melt.

The simulated fluid velocity in Al-7Si is two orders of magnitude higher than in SCN-0.24H_2O due to a stronger pore driven Marangoni convection. Table 5 compares the thermophysical properties of the Al-7Si and SCN-0.24 H_2O alloys.

Table 6 A comparison of the thermophysical properties of Al-7Si and SCN-0.24H_2O

Parameters	Labels	Units	SCN-0.24H_2O	Al-7Si	Reference (Al-7Si)
Eutectic Temp	T_e	K	292.15	850.15	35
Heat capacity	C_p	J/(kg.K)	2000	1070	3
Thermal Gradient	G	K/m	716	3200	This work
Thermal conductivity	K	W/(m.K)	0.222	76.7	3
Temperature derivative of surface tension	Υ	N/(m.K)	-0.082E-03	-0.2E-03	52
Primary Dendrite Arm Spacing	PDAS	μm	350	750	This work
Length of void	L	m	0.0013	0.011	This work
Density of fluid	ρ	kg/m^3	907	2408	3
Viscosity of fluid	μ	Pa.s	2.60E-03	1.16E-03	3
Liquidus Temp	T_l	K	329.35	892.82	35
Melting Point	T_m	K	331.39	946.15	35
Temp@Void_top	T_1	K	330.33	927.18	This work
Temp@Void_bottom	T_2	K	329.35	892.82	This work
Thermal Diffusivity	α = k/rho*Cp	m^2/s	1.22E-07	2.98E-05	This work
Marangoni No $=\frac{\text{Surface Tension Forces}}{\text{Viscous Forces}}$	$Ma = \frac{-\Upsilon * L * (T1 - T2)}{(\mu * \alpha)}$		328	1970	This work
Prandtl No = $\frac{\text{Momentum Diffusivity}}{\text{Thermal Diffusivity}}$	$Pr = \frac{Cp*\mu}{k}$		23	0.016	This work
Maximum Fluid Velocity	V	mm/s	0.5	120	This work
Growth speed	R	μm/s	5	40	This work
No. of cycles	V/R		100	3000	This work

From this table, it can be inferred that

- $\Upsilon_{Al\text{-}7Si} = 2.25 * \Upsilon_{SCN\text{-}0.24H2O}$
- $\alpha_{Al\text{-}7Si} = 250 * \alpha_{SCN\text{-}0.24H2O}$

- $Ma_{Al\text{-}7Si} = 3 * Ma_{SCN\text{-}0.24H2O}$
- $Pr_{Al\text{-}7Si} = 0.0007 * Pr_{SCN\text{-}0.24H2O}$

Thus, the thermal forces seem to dominate over viscous forces more significantly in the case of Al-7Si than in SCN-0.24H_2O. This is the reason for the significantly higher COMSOL simulated fluid speeds during directional solidification of Al-7Si.

Thus, for example in the case of Al-7Si alloy solidification of a 1.33 cm length at a growth speed of 40 μm/sec would require 332 sec. During this time the recirculating Marangoni flow with COMSOL simulated speed of 12 cm/sec will traverse ~3000 cycles through the upper permeable portion of the mushy-zone. This certainly would be more than sufficient to fragment a side arm especially during the initial remelting of the feed bar before starting its DS, as was the case with the MICAST2-12 sample at this sample location. The recirculating flow would follow the same clock wise motion and therefore via repeated impacts it would rotate such a fragmented side arm. This is evident from Fig. 39 which shows the misoriented dendrite grain marked by the yellow dotted line, which ultimately became a spurious grain observed in the MICAST-2-12 sample even though it was directionally solidified on the Space Station in the absence of gravity.

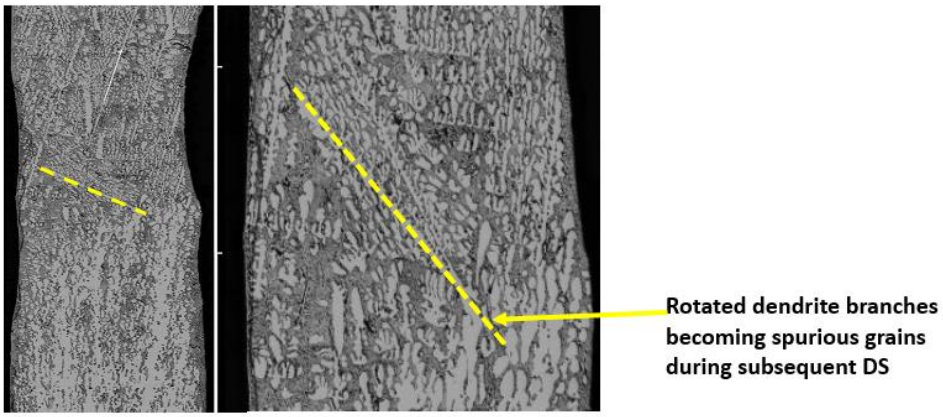

Figure 39 MICAST2-12 (Al-7Si) ISS (2016)

It is also very likely that other spurious grains observed in the MICAST-6, 7 and 12 samples at various locations may also have formed via this same mechanism, detachment of dendrite side-branch and its rotation caused by the Marangoni convection initiated by a pore existing at the melt-crucible interface. It reinforces the need to ensure that a mechanism such as spring-piston be incorporated within the crucibles during experiments where the aim is to completely eliminate terrestrial natural convection by carrying out solidification on the Space Station.

Chapter V

Summary and Conclusion

Al-7Si alloy samples, MICAST-6, MICAST-7 and MICAST2-12 directionally solidified on the International Space Station in a convection free $<10^{-4}$ g gravity environment were metallographically examined on the longitudinal sections parallel to the growth direction and on transverse sections cut at several places along their directional solidification length. Their examination indicated presence of voids at several locations on the sample surface where the melt was apparently detached from the crucible wall. Primary dendrite trunk diameters were measured on these samples, and those agree reasonably well with predictions from theoretical model which does not include convection in the melt. (Please note that these dendrite trunk diameter *results are presented in the Appendix-B, and they have not been included in the main body of thesis for the sake of clarity*.) This would have led us to conclude that these samples did solidify under purely diffusive transport conditions, as originally envisioned. However, examination of alignment of primary dendrites on the longitudinal and transverse sections from the directionally solidified portion of these samples showed several locations where it was completely different from that existing in the un-melted seed portion of these samples. This indicated

that “spurious grains” formed during solidification of these samples in the convection free low gravity environment of space. In a quiescent environment, the primary dendrite trees in an array are expected to maintain their original [100] alignment in the seed during the subsequent remelting and directional solidification of these feed-bars. Therefore, no spurious grains should be present in MICAST samples.

This led us to believe that Marangoni convection may have ensued on the free liquid-vapor surface in the melt where the melt column was detached from the crucible wall because the liquid-vapor surface energy in the Al-Si alloy decreases with increasing temperature. Under the presence of a positive thermal gradient in the melt, this surface-tension gradient would drive the Marangoni convection.

An examination of NASA-Microgravity experiments archive available via PSI-data base showed that directional solidification experiments were conducted on the Space Shuttle in 2002 on a transparent organic alloy (SCN-0.24H_2O) whose solidification is analogous to FCC metal alloys. Detailed analysis of the video data available from NASA on these PFMI (“Pore Formation and Migration Experiments”) experiments was undertaken to identify portions where solidification and dendrite array morphology was recorded especially in the presence of gas-pores adhered to the crucible wall in the melt column.

Fluid speeds associated with Marangoni convection in these PFMI samples were measured and also the fragmentation behavior of primary dendrite arms was recorded. These data clearly show that a surface bubble adhered to the crucible wall during directional solidification of a dendritic array creates a recirculating flow which brings in the warmer melt from ahead into the mushy-zone in its vicinity and also the flow while

coming back from the mushy-zone brings back solute rich melt in contact with the portions of the dendrite array which was already solidified. This leads to fragmentation and rotation of slender dendrite side-arms. Such broken fragments ultimately lead to formation and growth of spurious grains.

COMSOL software has been used to simulate Marangoni convection during directional solidification in the presence of a bubble adhered to the crucible wall for the processing conditions which simulate the SCN-0.24 H_2O and also the Al-7Si alloys. There is a qualitative agreement between the visually observed fluid flow patterns and those simulated by using a two-dimensional mesh and COMSOL. However, quantitative agreement is poor. The simulations indicate that surface adhered pore driven Marangoni flows would be much stronger in the case of Al-7Si alloys as compared with SCN-0.24H_2O. This suggests that the spurious grains observed in the MICAST alloys were indeed formed by such a Marangoni convection and reinforces the need to incorporate mechanism within the crucible which would keep the bulk melt column ahead always compressed on to the solidifying solid below and thus eliminate any solidification-shrinkage or dissolved gas induced pore formation. Only then purely diffusive transport conditions can be achieved during solidification on the Space Station.

Under this research, it has been seen that:

- Voids were present on the surface of all three MICAST samples which were solidified on the space station.
- All the three MICAST samples showed presence of spurious grains during metallographic investigation. The samples were not single crystal structure inspite

of undergoing DS in purely diffusive environment in space where there is no possibility of convection.

- Video of an organic transparent analogue of metals, SCN-0.24H_2O alloy, which solidifies in pattern similar to Al-7Si, undergoing directional solidification in space was chosen for further analysis.
- The video showed the presence of large bubble adhered on the crucible wall, few tracer bubbles traversing a circular path and disrupting the growing dendritic array.
- By measuring the velocity of two of the tiny tracer bubbles experimentally, it was seen that the fluid velocity increased on reaching the L-S interface towards the void and decreasing as it moves away from the interface into the bulk melt.
- Fluid with this small speed (~0.5mms^{-1}) traversing ~100 cycles within the mushy zone is sufficient to break the secondary arms of the dendrites. The video also showed the repeated impact of fluid circulation causing fragmentation and rotation of dendritic side arms. The fragments were rotating and falling off in absence of gravity instead of staying motionless.
- Simulation (COMSOL) of PFMI experiment showed similar trend in fluid velocity. However, simulated velocities are one order of magnitude smaller than experimentally measured velocity of tracer bubbles.
- This may be due to 2D simulation of 3D phenomenon. Velocity measurements in COMSOL is for the entire streamline while experimental measurement of velocity using the images of the PFMI video cannot take into consideration the fluid path which is in the mushy-zone below the array tips where the fluid velocity is comparatively much lesser.

- Both simulation and experimental results confirm the Marangoni convection due to the surface tension gradient induced by the void i.e. bubble adhered on the crucible during DS of SCN-0.24H_2O on space station.
- The voids on the MICAST samples must have caused the Marangoni convection to take place due to the surface tension gradient across the void.
- This must have caused the fragmentation and rotation of dendritic side arm in MICAST samples as found in SCN-0.24H_2O.
- Simulation (COMSOL) of Al-7Si alloy (MICAST-2-12) showed that the Void driven Marangoni convection resulted in average fluid velocity to decrease in the bulk liquid while a spike was observed when the fluid returns towards the void or L-S interface.
- However, simulated fluid velocity in Al-7Si is two orders of magnitude higher than that in SCN-0.24 H_2O due to larger thermal gradient across the void and better thermal diffusivity in Al-7Si.
- Fluid with a higher speed of ~120 mms^{-1} traversing ~3000 cycles is strong enough for causing dendritic arm fragmentation and rotation in different direction compared to the growing dendritic array.
- Thus, the final solidified MICAST sample showed spurious grains which may have nucleated from the fragmented side arms during directional solidification on the space station.

The results will help in advancing the field:

- In solidification processing by providing fundamental data, free of convective effects, for models and theory.
- In materials processing techniques by promoting our knowledge of void or bubble driven Marangoni Convection in low-gravity environments.

Chapter VI

Recommendations for Future Work

- A three dimensional simulation of the solidifying mushy-zone interacting with the Marangoni convection as the dendrite array approaches a pore created by surface detachment of melt column needs to be carried out.
- The simulations should include thermosolutal convection assisted remelting of dendrite side-arms causing their fragmentation.
- Simulations should also include a 'free body rotation' of fragmented arms in the presence of repeated impacts by the recirculting flow caused by Marangoni convection. Such simulations, if successful in predicting the exprimental observations presented in this study on the SCN-0.24H_2O (PFMI-experiments), in research can then be used to simulate solidification of metallic alloys, such as, Al-7Si. This would help explain in a quantitative manner the misaligments observed between dendrites in the seed portion and in the directionally solidified portion of MICAST-6, MICAST-7 and MICAST2-12 as part of this research.
- It is highly recommended to include some mechanism within the crucibles to ensure that the melt column is continually kept pressed onto the solid portion during

remelting and subsequent solidification to ensure that solidification occurs on the Space Station under purely diffusive transport condtitions.

References

1. Al-Rawahi N, Tryggvason G. Numerical simulation of dendritic solidification with convection: Three-dimensional flow. *Journal of Computational Physics*. 2004;194 (2):677-696. doi: http://dx.doi.org/10.1016/j.jcp.2003.09.020.
2. Dong H. Analysis of grain selection during directional solidification of gas turbine blades. *Proceedings of the World Congress on Engineering*. 2007.
3. Ghods M, Johnson L, Lauer M, Grugel RN, Tewari SN, Poirier DR. Radial macrosegregation and dendrite clustering in directionally solidified Al–7Si and Al–19Cu alloys. *Journal of Crystal Growth*. 2016;441:107-116. doi: http://dx.doi.org/10.1016/j.jcrysgro.2016.02.014.
4. Dong H, Dai H, Geblin J, et al. Grain selection during solidification in spiral grain selector. *Journal of the Minerals, Metals and Materials Society*. 2008:367-374.
5. Flemings M. *Solidification processing.* ; 1974.
6. Johnson L. *Analysis of microstructure and macrosegregation for directional solidification of Al-7 wt% Si alloy with A cross-section change at growth speeds of 10 and 29.1 μm/s.* Cleveland State University; 2012.
7. S. Angart, M. Lauer, S.N. Tewari, R.N. Grugel, D.R. Poirier: Comparison of directionally solidified samples solidified terrestrially and aboard the international space station, P*roceedings of 61st Annual Technical Conference of the Investment Casting Institute*, Covington, KY, Oct. 5 – 8, Paper 6, 2014.
8. M. Ghods, S.N. Tewari, M. Lauer, D.R. Poirier, R.N. Grugel: Processing parameter dependence of primary dendrite spacing and trunk diameter in Al-7 wt% Si alloy directionally solidified aboard the International Space Station, *American Society*

for Gravitation and Space Research Annual Meeting, Cleveland, OH, Oct 25-29, 2016. (https://ntrs.nasa.gov/archive/nasa/casi.ntrs.nasa.gov/20160013345.pdf)

9. J.R. Sarazin, A. Hellawell, "Channel formation in Pb–Sn, and Pb–Sb alloy ingots and comparison with the system NH4Cl – H2O," *Met. Trans. A, 1988* (19A) 1861-1871.
10. S.N. Tewari, R. Tiwari, G. Magadi: Mushy Zone Rayleigh Number to Describe Macrosegregation and Channel Formation in Directionally Solidified Metallic Alloys, *Metall. Materials Trans. 2004* (35A) 2927-2934.
11. M. Rappaz, Ch.-A. Gandlin, J.L. Desbiolles, Ph. Thevoz: Prediction of grain structures in various solidification processes, *Metall. Materials. Trans*. 27A (1996) 695-705.
12. Gandin, Ch-A., Michel Rappaz. "A coupled finite element-cellular automaton model for the prediction of dendritic grain structures in solidification processes." *Acta* Metall. Materialia 42.7 (1994): 2233-2246.
13. Ch.-A. Gandlin, J.L. Desbiolles, M. Rappaz, Ph. Thevoz: A Three-Dimensional Cellular Automaton–Finite Element Model for the Prediction of Solidification Grain Structures, Metall. Materials. Trans. 30A (1999) 3153-3165.
14. Lacdao C. *Influence of cross-section change during directional solidification on dendrite morphology, macrosegregation and defect formation in Pb-6 wt Sb Alloy.* Cleveland State University; 2017.
15. Grugel R., Brush L., Anilkumar A., *Disruption of an Aligned Dendritic Network by Bubbles during Re-melting in a Microgravity Environment*, 50th AIAA

Aerospace Sciences Meeting, 9 - 12 Jan 2012, 26th Symposium on Gravity - Related Phenomena in Space Exploration.

16. D. Poirier, P. Zhao and J. Heinrich, "Dendritic Solidification of Binary Alloys with Free and Forced Convection," Int. J. Numer. Meth. Fluids, vol. 49, pp. 233-266, 2005.
17. Karagadde, L. Yuan, N. Shevchenko, S. Eckert, P.D. Lee: 3-D microstructural model of freckle formation validated using in situ experiments, *Acta Materialia, 79* (2014) 168–180.
18. Shan Liu, Shu-Zu Lu, A. Hellawell: Dendritic array growth in the systems NH_4Cl–H_2O and $[CH_2\ CN]_2$–H_2O: the detachment of dendrite side arms induced by deceleration, *J. Crystal Growth* 234 (2002) 740–750.
19. R.H. Mathiesen, L. Arnmerg, P. Bleuet, and A. Somogyi: Crystal Fragmentation and Columnar-to-Equiaxed Transitions in Al-Cu Studied by Synchrotron X-Ray Video Microscopy, *Metall. Materials. Trans*. 37A (2006) 2515-2524.
20. D. Ruvalcaba, R.H. Mathiesen, D.G. Eskin, L. Arnberg, L. Katgerman: In situ observations of dendritic fragmentation due to local solute-enrichment during directional solidification of an aluminum alloy, *Acta Materialia* 55 (2007) 4287–4292.
21. W Xuan, Z Ren1, C Li, W Ren, C Chen: Formation of stray grain in cross section area for Ni-based superalloy during directional solidification, *Materials Sci. Eng*. 27 (2011) 012035 doi:10.1088/1757-899X/27/1/012035.

22. Kermanpur, A., et al.: Thermal and grain-structure simulation in a land-based turbine blade directionally solidified with the liquid metal cooling process. *Metall. Materials Trans.* 31 (2000) 1293-1304.
23. A. Kumar, P. Dutta: A Rayleigh number based dendrite fragmentation criterion for detachment of solid crystals during solidification, *J. Phys. D: Appl. Phys*. 41 (2008) 155501 (9pp).
24. The Marangoni Effect: A Fluid Phenom (March 10, 2011) Retrieved from https://www.nasa.gov/mission_pages/station/research/news/marangoni.html
25. Wikipedia contributors, "Marangoni effect," *Wikipedia, The Free Encyclopedia*, https://en.wikipedia.org/w/index.php?title=Marangoni_effect&oldid=839041233 (accessed May 14, 2018)
26. Wikipedia contributors, "Navier–Stokes equations," *Wikipedia, The Free Encyclopedia*, https://en.wikipedia.org/w/index.php?title=Navier%E2%80%93Stokes_equations&oldid=823105568 (accessed April 6, 2018).
27. JM Drezet, S Mokadem: Marangoni convection and fragmentation in laser treatment, *Materials Science Forum* vol. 508 (February 2006) pp. 257-262.
28. T.D. Anderson, J.N. Dupont, T. Debroy: Stray grain formation in welds of single-Crystal Ni-base superalloy CMSX-4, *Metall. Materials Trans A*, 41A (2010) 181-193.
29. R Acharya, R Bansal, JJ Gambone, S Das: A coupled thermal, fluid flow, and solidification model for the processing of single-crystal alloy CMSX-4 through scanning laser epitaxy for turbine engine hot-section component repair (Part I), *Metall. Materials Trans. B*, 45 (2014) 2247–2261.

30. A Basak, R Acharya, S Das: Additive manufacturing of single-crystal superalloy CMSX-4 through scanning laser epitaxy: computational modeling, experimental process development, and process parameter optimization, Metall. Materials Trans. A, 47 (2016) 3845–3859
31. Richard Grugel and A Anilkumar. "Bubble Formation and Transport During Directional Solidification in Microgravity: Model Experiments on the Space Station", 42nd AIAA Aerospace Sciences Meeting and Exhibit, Aerospace Sciences Meetings, https://doi.org/10.2514/6.2004-627
32. PSI-PFMI Video-15.
33. S. Angart, M. Lauer, S.N. Tewari, R.N. Grugel, D.R. Poirier: Comparison of directionally solidified samples solidified terrestrially and aboard the international space station, P*roceedings of 61st Annual Technical Conference of the Investment Casting Institute*, Covington, KY, Oct. 5 – 8, Paper 6, 2014.
34. Lauer, M., Ghods, M., Angart, S.G. et al. JOM (2017) 69: 1289. https://link.springer.com/article/10.1007/s11837-017-2380-0
35. Rajamure, Ravi Shanker, "Directional Solidification of Al - 7 WT Si Alloy" (2010). ETD Archive. Paper 753.
36. Tewari SN, Grugel RN, Poirier DR. An evaluation of primary dendrite trunk diameters in directionally solidified Al-Si alloys. *Journal of Light Metals*. 2014; 45(11):4758-4761.
37. Glicksman, M.E., Schaefer, R.J., Ayers, J.D.: Dendritic growth – A test of theory. *Metall. Trans. A* 7A, 1747–1759 (1976)

38. Glicksman, M.E., Koss, M.B., Bushnell, L.T., LaCombe, J.C., Winsa, E.A.: Dendritic growth of succinonitrile in terrestrial and microgravity conditions as a test of theory. *ISIJ Int. 35*, 1216 (1995)
39. Lupulescu, A., Glicksman, M.E., Koss, M.B.: *42nd AIAA Aerospace Sciences Meeting and Exhibit*. AIAA 2004-626 (2004)
40. Richard N. Grugel, Lucien N. Brush, Amrutur V. Anilkumar, Disruption of an Aligned Dendritic Network by Bubbles During Re-melting in a Microgravity Environment, Microgravity Science and Technology, 2012, Volume 24, Number 2, Page 93
41. R. Balasubramaniam and J.E. Lavery: Num. Heat Transfer 1989, vol. A 16, p. 175.
42. Boehm-Courjault E. et al, "EBSD: a powerful microstructure analysis technique in the field of solidification" *Journal of Microscopy*, Vol. 233, Pt 1 2009, pp. 160–169
43. P. L. Mills, K. Barman , S. Mothupally, A. Sonejee, *Fluid Motion Between Rotating Concentric Cylinders Using COMSOL Multiphysics® Software*, Texas A&M University - Kingsville, Kingsville, TX, USA
44. Alireza Bahrami, Daryush K. Aidun, *Modeling of Transport Phenomena in Gas Tungsten Arc Welding of Ni to 304 Stainless Steel*, MAE Department, Clarkson University
45. A. Amiri and K. Vafai, "Transient Analysis of Incompressible Flow Through a Packed Bed," *Int. J. Heat and Mass Transfer*, vol. 41, pp. 4259–4279, 1998.

46. Wikipedia contributors, “Darcy’s law,” Wikipedia, the Free encyclopedia, https://en.wikipedia.org/w/index.php?title=Darcy%27s_law&oldid=832019504 (accessed April 17, 2018).
47. P. Tin, H. C. de Groh III, Surface Tension and Viscosity of Succinonitrile– Acetone Alloys Using Surface Light Scattering Spectrometer, *International Journal of Thermophysics*, 2004, Volume 25, Number 4, Page 1143
48. Beckermann, C., "Measurement of the Density of Succinonitrile-Acetone Alloys," *J. Crystal Growth*, Vol. 222, 2001, pp. 380-391,
49. W.F. Kaukler and D.O. Frazier: J. Cryst. Growth, 1985, vol. 71, pp. 340-45.
50. Wikipedia contributors, "Scheil equation," Wikipedia, The Free Encyclopedia, https://en.wikipedia.org/w/index.php?title=Scheil_equation&oldid=827764268 (accessed April 17, 2018).
51. Transport Phenomena in Metallurgy, G.H. Geiger and D.R. Poirier, eds., *Addison-Wesley Publishing Company*, New York, NY, 1973, p. 92.
52. S. N. Tewari and R. Tiwari: *Metall. Mater. Trans. A*, 2003, vol. 34A, pp. 2365-76
53. V. Sklyarchuk, Yu. Plevachuk, A. Yakymovych, S. Eckert, G. Gerbeth, K. Eigenfeld, Structure Sensitive Properties of Liquid Al–Si Alloys, *International Journal of Thermophysics*, 2009, Volume 30, Number 4, Page 1400

Appendix A: Orientation Measurements

(Macro Code)

```
fname=File.openDialog("Select image");
open(fname);
title=getTitle;
run("RGB Color");
H1=getHeight();
W1=getWidth();
selectWindow(title);
close();

newImage("Image", "RGB white", W1, H1, 1);

fname=File.openDialog("Select ROIset");
roiManager("Open",fname);
N=roiManager("count");

fname=File.openDialog("Select ROIset Boundaries");
roiManager("Open",fname);
M=roiManager("count");
Y=M-N;

for(i=0;i<(N/2);i++)
{
roiManager("Select",2*(i));
getLine(p1, q1, p2, q2, lineWidth);
dp1=p2-p1;
dq1=q2-q1;
m1=dq1/dp1;
c1=q1-m1*p1;


roiManager("Select",(2*i)+1);
getLine(x1, y1, x2, y2, lineWidth);
dx2=x2-x1;
dy2=y2-y1;
m2=dy2/dx2;
c2=y1-m2*x1;


X=(c2-c1)/(m1-m2);
Y=m1*X+c1;

b=((x2-X)*(x2-X))+((y2-Y)*(y2-Y));
l=((sqrt(b))*1000/596);
a=((x2-x1)*(x2-x1))+((y2-y1)*(y2-y1));
k=((sqrt(a))*1000/596)-l;
if(k<l)
```

```
{
A=k;
B=l;
}
else
{
A=l;
B=k;
}

d=((p2-X)*(p2-X))+((q2-Y)*(q2-Y));
n=((sqrt(d))*1000/596);
c=((p2-p1)*(p2-p1))+((q2-q1)*(q2-q1));
m=((sqrt(c))*1000/596)-n;
if(m<n)
{
C=m;
D=n;
}
else
{
C=n;
D=m;
}

aa=A+B;
bb=C+D;

if(aa<bb)
{
A1=A;
B1=B;
C1=C;
D1=D;
}
else
{
A1=C;
B1=D;
C1=A;
D1=B;
}

Z1=atan(-m1);
Z2=atan(-m2);

angle1=Z1*(180/PI);
angle2=Z2*(180/PI);

if(angle1<0)
{
```

```
theta1=180+angle1;
}
else
{
theta1=angle1;
}

if(angle2<0)
{
theta2=180+angle2;
}
else
{
theta2=angle2;
}

if(theta1<=90)
{
Alpha=theta1;
Beta=theta2;
}
else
{
Alpha=theta2;
Beta=theta1;
}

if(0<theta1 && theta1<=90)
{
orientation=theta1;
}
else
{
orientation=theta2;
}

Difference=Beta-Alpha;
RSD=A1/B1;
RLD=C1/D1;
LSD=A1+B1;
LLD=C1+D1;
RD=(LSD)/(LLD);
i=nResults;
setResult("X",i,X);
setResult("Y",i,Y);
setResult("A (µm) ",i,A1);
setResult("B (µm) ",i,B1);
setResult("C (µm) ",i,C1);
setResult("D (µm) ",i,D1);
setResult("a in Degrees",i,Alpha);
setResult("ß in Degrees",i,Beta);
```

```
setResult("a  - ß in Degrees",i,Difference);
setResult("Dendrite Orientation in Degrees",i,orientation);
setResult("A/B",i,RSD);
setResult("C/D",i,RLD);
setResult("A+B",i,LSD);
setResult("C+D",i,LLD);
setResult("(A+B/C+D)",i,RD);
print(nResults);

for(j=N;j<M;j++)
{
roiManager("Select",j);
name=Roi.getName;
inside=Roi.contains(X,Y);
if(inside==1)
{
setResult("grain",i,name);
}
}
updateResults();
}
for(i=0;i<(N/2);i++)
{
Grainno=getResult("grain",i);
if(Grainno==1)
{
roiManager("Select",(2*i));
setForegroundColor(085, 000, 093);
run("Fill", "slice");
roiManager("Select",((2*i)+1));
setForegroundColor(085, 000, 093);
run("Fill", "slice");
}
else if(Grainno==2)
{
roiManager("Select",(2*i));
setForegroundColor(255, 0, 0);
run("Fill", "slice");
roiManager("Select",((2*i)+1));
setForegroundColor(255, 0, 0);
run("Fill", "slice");
}
else if(Grainno==3)
{
roiManager("Select",(2*i));
setForegroundColor(0, 255, 0);
run("Fill", "slice");
roiManager("Select",((2*i)+1));
setForegroundColor(0, 255, 0);
run("Fill", "slice");
}
```

```
else if(Grainno==4)
{
roiManager("Select",(2*i));
setForegroundColor(0, 0, 255);
run("Fill", "slice");
roiManager("Select",((2*i)+1));
setForegroundColor(0, 0, 255);
run("Fill", "slice");
}
else
{
roiManager("Select",(2*i));
setForegroundColor(255, 0, 255);
run("Fill", "slice");
roiManager("Select",((2*i)+1));
setForegroundColor(255, 0, 255);
run("Fill", "slice");
}
}

for(j=N;j<M;j++)
{
roiManager("Select",j);
name=Roi.getName;
linewidth = 10;
setLineWidth(linewidth);
if(name==1)
{
setForegroundColor(085, 000, 093);
run("Draw", "slice");
}
else if(name==2)
{
setForegroundColor(255, 0, 0);
run("Draw", "slice");
}
else if(name==3)
{
setForegroundColor(0, 255, 0);
run("Draw", "slice");
}
else if(name==4)
{
setForegroundColor(0, 0, 255);
run("Draw", "slice");
}
else
{
setForegroundColor(255, 0, 255);
run("Draw", "slice");
}
```

```
}
selectWindow("Log");
run("Close");
saveAs("Tiff");
saveAs("Measurements");
selectWindow("ROI Manager");
run("Close");
selectWindow("Results");
run("Close");
```

Appendix B: Measured Vs Predicted Results for MICAST Samples

A] Trunk Diameter: Measured Vs Predicted